Application of high-order edge elements and PML to horn antenna analysis

Prakash Paul

Department of Electrical and Computer Engineering
McGill University
Montreal, Canada

August 2003

A thesis submitted to the Faculty of
Graduate Studies and Research
in partial fulfillment of the requirements of
the degree of Master of Engineering

Your file Votre référence
ISBN: 0-612-98556-3
Our file Notre référence
ISBN: 0-612-98556-3

Table of Contents

Table of Figures

Acknowledgements

I would like to express my sincere respect and gratitude to my supervisor, Professor Jonathan P. Webb, for his guidance and financial support in the accomplishment of this Master's thesis. This work would not have been completed without his keen insights and ability to remain focused on our vision of the project. I consider myself privileged to have had him as my thesis supervisor.

I would like to thank to my parents, Jogesh and Kamala Paul. I owe them the most. Their love, faith, continuous interest and constant care were strongly felt at all the times regardless of the distance. I thank them from the bottom of my heart. As the key figures in my life, I do not think there is a more appropriate circumstance to acknowledge that all you have done for me Ma and Baba. I am forever indebted to you.

To my brothers, Subodh, Dilip, Pradip, and Ashutosh Paul, and to my sister Dipty Paul, and their families, I owe a huge debt of gratitude. I thank them for having constant faith in me and for being the amazing role models that they are.

Last but not least, I would like to thank my colleagues from the CADLab for their friendship, cooperation, and the pleasant working environment they helped to create. Thank you all for the encouragement and energy. You were the ones who stayed right by me when I needed it most. Special thanks to Dileep Nair for his advice and proof reading my report, Wissam Saliba for helping me with the MFC, and Elias Tochtamis for translating the abstract in French.

Abstract

There are many methods for truncating finite element (FE) meshes for unbounded problems. Among them the Perfectly Matched Layer (PML) is the most promising. In this thesis, application of the PML to a high-order FE method is investigated, particularly with respect to its ability to analyze horn antennas.

The anisotropic material properties of the PML can be chosen such that a plane-wave incident from free space onto the anisotropic material will have no reflection. The interface of the absorber is made reflectionless by choosing the appropriate ε and μ values to be complex diagonal tensors. The performance parameters of this absorber are explored.

For the finite element analysis, high-order hierarchal edge elements are used, and how the element size and order of the basis function affect the solution accuracy and computational cost are observed. It is possible to achieve very good absorption for comparatively less computational cost by using relatively thin absorbing layers along with careful consideration of the relations of the element size and the order of the basis function. The impedance characteristics and far field radiation pattern of a horn antenna are computed and compared with previously-published measured results.

Abstrait

Il y a beaucoup de méthodes pour tronquer les mailles d'éléments finis (EF) pour les problèmes qui sont illimités. Entre elles, la Couche Parfaitement Egalée (CPE) est la plus prometteuse. Dans cette thèse, l'application du CPE à la méthode EF haut ordre est examinée, particulièrement par rapport à sa capacité pour analyser les antennes de corne.

Les propriétés matérielles anisotropes du CPE peuvent être choisies tel qu'un incident de "plane-wave" qui provient de l'espace libre sur le matériel anisotrope n'aura pas de reflet. L'interface de l'absorbeur est faite sans reflet en choisissant les valeurs correspondantes μ et ε pour être des tenseurs diagonaux complexes. Les paramètres d'exécution de cet absorbeur sont explorés.

Pour l'analyse d'éléments finis, les éléments d'haut ordre hiérarchique de bord sont utilisés, et comment la taille et l'ordre de la fonction de base affectent la précision de solution et le coût de calculs ont été observés. C'est possible d'atteindre une très bonne absorption pour un coût de calculs comparativement moins en utilisant des couches absorbant relativement minces avec une considération prudente des relations de la taille d'élément et l'ordre de la fonction de base. Les caractéristiques d'impédance et le modèle de rayonnement de champs lointain d'une antenne de corne sont calculés et comparés avec les résultats déjà mesurés dans des publications précédemment publiées.

1 Introduction

1.1 Problem Description

Reflector antennas widely use horns as their primary feed. The purpose of the horn in an ideal reflector is to transform the angular distribution of energy emerging from the feed into a spatial distribution across the aperture which leads to the desired far-field radiation pattern. To predict the performance of a reflector antenna, accurate characterization of the feed horn is important.

In the 1950's, reflector antennas became widely used in terrestrial microwave communication systems. Reflector antennas for satellite communications and radio astronomy require high performance feeds. In 1962, Kay [1] proposed an idea of using corrugated horn for radiating a symmetrical radiation pattern. Subsequently, the horn was shown to radiate with a very low level of cross polarization, which is essential for dual-polarized systems. As a consequence, the horn has become the prime choice for high performance reflector antennas.

The shape and characteristics of the radiation pattern of a feed are the most important parameters as these directly influence the fields which are directed at a reflector, thus determining the radiation characteristics of the whole antenna. The frequency of operation of an antenna, its bandwidth, the voltage standing wave ratio, beamwidth and gain are among the key parameters which determine the size of the horn. Usually horns have diameters in the range of 40 -100 wavelengths and operate at frequencies above 1GHz. The reflection coefficient and return loss are the other significant performance parameters in communication and radar systems. Return loss is normally set below -30dB for these practical applications [2].

There are a number of numerical methods that have been used to solve for the fields radiating from a horn. Among them, the finite element method (FEM) leads to very

sparse system matrices and can be quickly solved by using iterative techniques, and is less demanding on computer storage. However, without some method to truncate the problem space, the FEM technique would require meshing of the infinite space surrounding the conducting body. The anisotropic-material based Perfectly Matched Layer (PML) [3] is very effective for scattering problems, provided that appropriate material properties and geometry of the PML are used.

In this thesis, an investigation of the Anisotropic PML in the context of the FEM is presented and compared with the measured results [4].The main interest for the PML in the present case is to use it to absorb the scattered field from a Horn Antenna in free space. Thus the PML material must almost totally surround the horn.

1.2 Literature Survey

1.2.1 Analysis Methods for Horn Antenna

The classical method of studying the internal region of a horn, also known as the simple modal approach, is to predict the modal characteristics which describe the fields in the aperture. The simple modal approach is a computer method for analyzing horn antennas in which the actual profile of the horn is replaced by a series of uniform waveguide sections. This method works well when the fields are stable along the horn and the aperture fields are composed of either one or two discrete modes [5]. However, there are two restrictions on the method: first, it does not predict the consequences of discontinuities along the horn which will lead to the excitation of multiple modes. Second, it gives no information on the impedance properties of the horn. Yet, both these restrictions can be overcome by using the modal matching technique which aims to predict precisely how the fields vary at all points along the horn. However, this is done at the expense of a complicated analysis and lengthy computational process.

The modal matching technique requires matching the total modal field at each junction between uniform sections so that conservation of power is maintained. The power of modal matching technique stems from the fact that the amplitudes of the mode can be

expressed as the components of a scattering matrix. Each junction along the horn has its own scattering matrix. The matrix for all junctions are cascaded and an overall scattering matrix is derived, which will contain the input reflection coefficients and the output transmission coefficients, from which the aperture fields are computed. Unfortunately, modal matching techniques can not be applied to an arbitrary shaped horn. If the shape of the horn aperture can not be expanded as an orthonormal set of modes [6], a numerical point-by-point technique must be used.

There are a number of numerical methods that may be used to solve for the fields radiated from an arbitrary horn. Two of the most popular methods are: the MoM [7], and the FEM [8]. Each of these methods have associated advantages and disadvantages. The MoM lends itself well to the open-region for very simple geometrical problems in that it involves the discretization of the surface of the object only. However, it gets very expensive as the geometrical complexity of the device grows, and especially if dielectrics are involved. The MoM also leads to a full-system matrix, which requires extensive computer resources for storage and solving. On the other hand, the FEM leads to a very sparse system matrix that is quickly solved using iterative techniques and is less demanding on computer storage. Without some method to truncate the problem space, the FEM technique would require meshing of the infinite space surrounding the conducting body. Several truncation methods have been studied in previous works, some of which are presented below.

1.2.2 Truncation Methods

To predict the radiation pattern of a horn using the FEM, it is necessary to assign an artificial finite boundary that will represent the infinite free space. This is a very active research area and several interesting approaches have been proposed. Among them the Robin Absorbing Boundary Condition (ABC), the Hybrid FEM and the Boundary Element Method (BEM), and the PML hold the most promise [9].

The Robin ABC can be viewed as the combination of classical 1st order ABC and the

integral equation method. Remarkable results have been shown using this approach. However, the iterative process makes it very expensive and there is no guarantee that it will converge for all electromagnetic problems [10].

The hybrid FEM and BEM is an exact mesh truncation method [11]. The major drawbacks of this approach are: since the truncation boundary is handled through the BEM, dense and non-symmetric matrix blocks are created; and for different configurations and applications appropriate Green's functions need to be derived and implemented.

The interface between the PML and free space is reflection-less for all frequencies, polarizations, and angles of incidence. Two types of PML are well-known: the split-Field formulation, introduced by Berenger [12], and the anisotropic material based PML by Sacks et al. [13]. Berenger's PML requires modification of Maxwell's equations to allow for the specification of material properties which result in a reflection-less lossy material. Although Berenger demonstrates the validity of his approach with numerical experiments, the physical meaning of his modifications to Maxwell's equations is not very clear. The anisotropic material based PML provides a better physical understanding of the PML because it can be explained within the frame-work of Maxwell's equation. Another advantage of the anisotropic PML is that the FEM is well developed for Maxwell's equations [13].

Recently, Bardi and Cendes [14] have automated the PMLs for unbounded scattering problems and used them together with *h*-adaption mesh refinement so that the tetrahedral elements in the PML regions can be adjusted according to the numerical solution. In this way, extra overhead due to PMLs can be kept to a minimum. Very impressive results have been obtained, but occasionally non-physical resonances in the PML regions can contaminate the solution within the problem domain.

1.2.3 High-order Edge Elements

The tetrahedral element is the simplest tessellation shape capable of modeling arbitrary three-dimensional geometries, and is well suited for automatic mesh generation [18]. Edge elements are used because node-based elements encounter serious problems when trying to represent vector electric or magnetic fields. Spurious modes are observed when modeling cavity problems using node-based elements. Nodal bases also require special care for enforcing boundary conditions at material interfaces, conducting surfaces, and geometry corners [15]. By using higher order polynomials greater accuracy can be achieved with the same number of tetrahedrons. By using *hierarchal* high-order elements, different orders can be used together in the same mesh. So, *p*-adaption is possible.

1.3 Outline

A brief description of the FEM is presented in chapter 2. Special attention is given to the Hierarchal High-Order Edge Element since this is the element used in this work.

In chapter 3, the behavior of waves in an Anisotropic PML is introduced. The details of calculating the material properties for the PML box are presented. How the dimensions of the PML box and the properties of the PML material affect the performance of the FEM solver is also discussed.

Chapter 4 outlines the implementation of the computer program for automating the PML box and its material properties. The different input and output parameters used in the program are discussed briefly. A technique for evaluating far field is also presented.

In chapter 5, the results of the investigative studies are presented. As a preliminary study to confirm that the PML is working properly, the short-circuited and PML-Ended parallel plate waveguide and rectangular waveguide were considered. The normalized aperture impedance for a waveguide with flange in a rectangular PML Box, and the return loss of a horn antenna in a PML Box were investigated next. Finally, far field radiation pattern

of a horn was observed.

Chapter 6 presents some important conclusions from this study, and briefly discusses possible future work in the area.

2 Hierarchal High-Order Edge Element

2.1 Finite Elements

The finite element method (FEM) is a numerical technique for obtaining approximate solutions to boundary-value problems in mathematical physics and engineering. FEM has been recognized as a general method with wide applications in electromagnetics. Two classical methods, the Ritz variational method and the Galerkin's method, form the basis of modern FEM [8]. In the classical Ritz and Galerkin methods, the trial function is formulated as a combination of a set of basis functions defined over the entire solution domain, which is capable of representing, at least approximately, the true solution of the problem. For many problems this is very difficult, if not impossible, and this is true particularly for two- and three-dimensional problems. To alleviate this problem, the entire domain is divided into small subdomains and trial functions are defined over each subdomain. Since the subdomains are small, the trial functions, which are a combination of the set of basis functions, are usually in a much simpler form. The procedure that employs the Ritz method is usually referred to as the Ritz FEM, or better known as the variational FEM, whereas the one that employs Galerkin's method is usually referred to as the Galerkin FEM.

After discretizing the problem domain, suitable interpolation polynomials, also referred to as shape or basis functions, are used to approximate the unknown function within each element. Once the basis functions are chosen, it is possible to write a program to analyze complicated geometries. In this chapter, node-based and edge-based basis functions for two- and three-dimensional finite elements will be discussed. The hierarchal nature of the edge-based functions and their applications in p-based refinement techniques will also be discussed. At the end of this chapter, a brief description of the variational method is presented.

2.2 Node-Based High Order Elements

In node-based finite elements, the form of the unknown function E^e in the element is controlled by function values at its nodes. If the function values E_i^e at the nodes are taken as nodal variables, then the approximating function for an element e with n nodes has the form

Equation 2-1
$$E^e = \sum_{i=1}^{i=n} E_i^e \zeta_i^e$$

The basis function ζ_i^e must be unity at node i and zero at all remaining nodes within the element.

Basis functions can be derived either by inspection (Serendipity family) or through simple products of appropriate polynomials (Lagrange family) [16]. It is easier and more systematic to construct higher order bases using Lagrange polynomials, while progression to higher orders is difficult in the Serendipity family. However, Lagrange basis functions have undesirable interior nodes and more unknowns than Serendipity basis functions of the same order.

2.2.1 Two-Dimensions

Two-dimensional finite elements have found widespread use in the modeling of structures whose third dimension is significantly larger or smaller than the cross section, thus ensuring little variation of the unknown parameters in the third direction. Two-dimensional finite elements have also been used to obtain reliable estimates of three-dimensional problems since the computational cost for obtaining two-dimensional solutions is lower than that for three dimensions. Another class of problems that can be analyzed using the two-dimensional finite element method is that of axisymmetric problems [8]. Unlike the two-dimensional geometries, which do not exist in reality, the axially symmetric geometries, also known as bodies of revolution, not only exist but are also very common. In 2-D, the subdomains could be triangles, rectangles, or 2-D curvilinear shaped elements, as shown in Figure 2-1. Triangular elements are the most

popular because they can model any arbitrary geometry. The basis functions of triangular elements using Lagrange interpolation polynomials will be determined here.

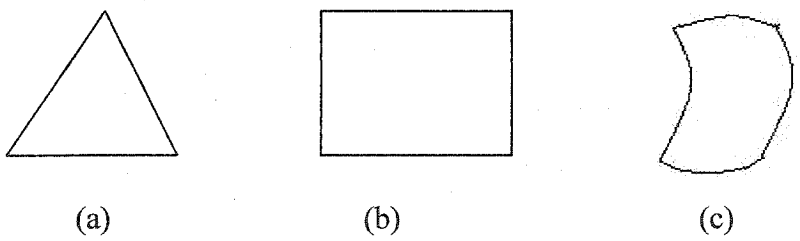

Figure 2-1: 2-D Elements. (a) Triangle (b) Rectangle (c) Curvilinear Element

Consider a point P within a triangular element shown in Figure 2-2. The area coordinates [8] L_i^e are given by

Equation 2-2
$$L_i^e = \frac{\Delta_i}{\Delta} \qquad i = 1,2,3$$

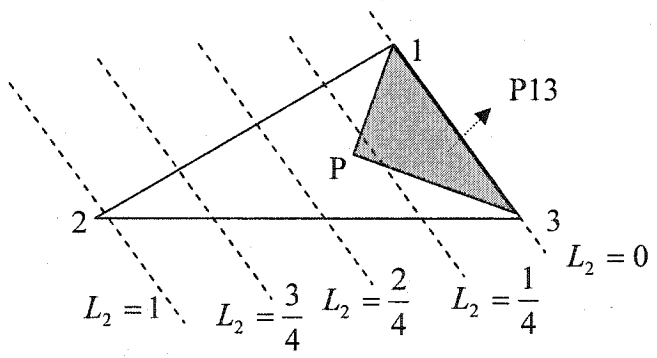

Figure 2-2: Area coordinates for a triangular element [15]

where Δ is the area of the whole triangle 123, Δ_1 is the area of triangle P23, Δ_2 is the area of triangle P13, and Δ_3 is the area of triangle P12. The coordinate L_i^e is zero on the edge opposite to vertex i and unity at vertex i. With the area coordinates defined above, we can easily construct the basis functions for a general triangular element. The expression for the basis function ζ_i^e associated with node i, labeled with (I,J,K), can be written as

Equation 2-3
$$\zeta_i^e = \mathrm{P}_I^p\left(L_1^e\right)\mathrm{P}_J^p\left(L_2^e\right)\mathrm{P}_K^p\left(L_3^e\right)$$

$$I + J + K = p$$

where p is the order of the basis function and $\mathrm{P}_I^p\left(L_1^e\right)$ denotes the polynomial defined as

Equation 2-4

$$\mathrm{P}_I^p\left(L_1^e\right)=\frac{1}{I!}\prod_{s=0}^{I-1}\left(pL_1^e-s\right) \qquad I>0$$

$$\mathrm{P}_0^p=1 \qquad I=0$$

and $\mathrm{P}_J^p\left(L_2^e\right)$ and $\mathrm{P}_K^p\left(L_3^e\right)$ are defined similarly.

In order to guarantee solution isotropy the polynomial expression must be a complete polynomial; that is, it must contain all together $m=\frac{1}{2}(p+1)(p+2)$ terms [8]. Consequently, there are m unknown coefficients and m nodes must be placed within the element. For the solution to be continuous, it is required to place one node at each of the three vertices of the triangle, $p-1$ nodes along each of its three edges, and the rest in the interior of the element.

For an example, consider the linear element shown in Figure 2-3:

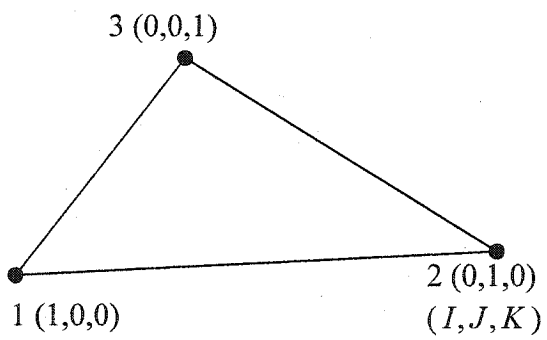

Figure 2-3: Numbering scheme for linear (p =1) element

$$p = 1$$
$$P_1^1\left(L_i^e\right) = L_i^e$$

Equation 2-5

$$\zeta_1^e = \mathrm{P}_1^1\left(L_1^e\right)\mathrm{P}_0^1\left(L_2^e\right)\mathrm{P}_0^1\left(L_3^e\right) = L_1^e \quad \textbf{using Equation 2-4 and Equation 2-3}$$
$$\zeta_2^e = \mathrm{P}_0^1\left(L_1^e\right)\mathrm{P}_1^1\left(L_2^e\right)\mathrm{P}_0^1\left(L_3^e\right) = L_2^e$$
$$\zeta_3^e = \mathrm{P}_1^1\left(L_1^e\right)\mathrm{P}_0^1\left(L_2^e\right)\mathrm{P}_1^1\left(L_3^e\right) = L_3^e$$

From this example, it can be seen that using this approach the construction of the interpolation functions is indeed very convenient.

2.2.2 Three-dimensions

While some physical problems can be represented or approximated by a one- or two-dimensional mathematical model, all physical problems are three-dimensional by nature. In 3-D, the subdomains could be tetrahedral, hexahedral or 3D curvilinear shaped elements, as shown in Figure 2-4. The tetrahedral element is the simplest tessellation shape capable of modeling arbitrary three-dimensional geometries, and is also well suited for automatic mesh generation. The basis functions of tetrahedral elements by using Lagrange interpolation polynomials will be determined here.

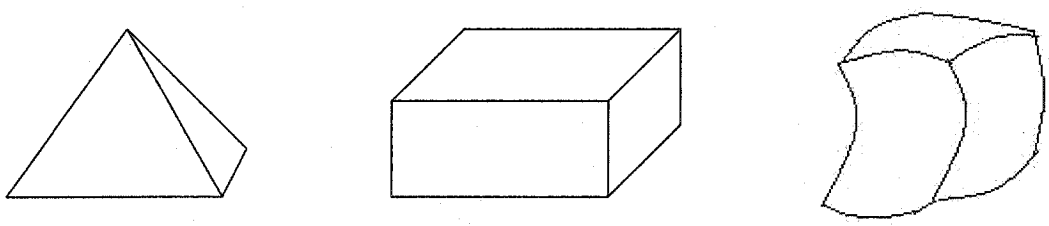

Figure 2-4: 3-D Elements. (a) Tetrahedral, (b) Hexahedral, and (c) Curvilinear Element

Consider a point P within a tetrahedral element shown in Figure 2-5. The volume coordinates [8] L_i^e is given by

Equation 2-6

$$L_i^e = \frac{\Delta_i}{\Delta} \qquad i = 1,2,3,4$$

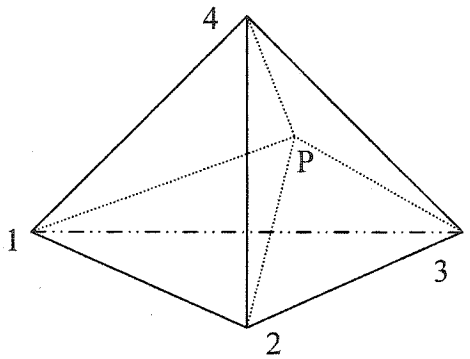

Figure 2-5: Point P within a tetrahedral element

where Δ is the volume of the whole tetrahedron 1234, Δ_1 is the volume of tetrahedron P234, Δ_2 is the volume of tetrahedron P134, Δ_3 is the volume of tetrahedron P124, and Δ_4 is the volume of tetrahedron P123 . The coordinate L_i^e is zero on the edge opposite to vertex i and unity at vertex i. As for the triangular elements, linear $(p=1)$ basis functions are equal to the volume coordinates

Equation 2-7 $$\zeta_i^e = L_i^e \qquad i = 1,2,3,4$$

2.2.3 High-order Node-Based elements

Linear elements, also referred to as first order elements $(p=1)$, have certain advantages and disadvantages. The main advantages are the simplicity of the formulation and the narrow bandwidth of the system equations [8]. The main disadvantage of the linear elements is the poor accuracy and slow convergence of the solution with respect to the number of elements. In principle, one can always increase the number of elements to achieve the desired accuracy. However, this is at the price of increasing computing time and memory demand.

An alternative approach to achieve higher accuracy without increasing the number of elements is to employ higher order basis functions or higher-order elements. The main disadvantages in using higher-order elements are the complexity of the formulation, and an increase in the bandwidth of the system equations. However, this approach has proven

to be very cost effective.

For example, if a six node quadratic $(p=2)$triangular element is constructed as in Figure 2-6 and Equation 2-4 is used

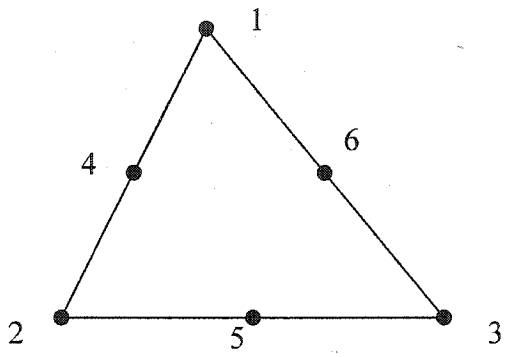

Figure 2-6: Six node quadratic triangular element

$$\zeta_1^e = L_1(2L_1 - 1)$$
$$\zeta_2^e = L_2(2L_2 - 1)$$
$$\zeta_3^e = L_3(2L_3 - 1)$$
$$\zeta_4^e = 4L_1L_2$$
$$\zeta_5^e = 4L_2L_3$$
$$\zeta_6^e = 4L_3L_1$$

2.3 Edge-based elements

The basis functions for the traditional node-based finite elements are scalar and they are associated with the nodes of the finite element meshes, which was explained in section 2.2 as node based basis functions. When they are applied to the vector problems, the natural approach is to divide the vector field into components and simply treat each component as a scalar. However, serious problems are encountered when node-based elements are employed to represent vector electric and magnetic fields. First, spurious modes are observed when modeling cavity problems using node-based elements [15]. Nodal basis functions impose continuity in all three spatial components whereas edge bases guarantee continuity only along the tangential component. Webb in [17] provides an explanation as to why spurious modes do not appear with edge elements. Second,

nodal bases require special care for enforcing boundary conditions at material interfaces, and corners. Edge-based finite elements, whose degrees of freedom are associated with the edges and the faces of the finite element mesh, have been shown to be free of the above shortcomings.

2.3.1 Two-Dimensions

Since the edges of an arbitrary triangular element are not parallel to the x- or y-axis, it is not easy to guess the form of the vector basis function by inspection. Therefore, the vector basis for a triangular element will be expressed in terms of its area coordinates, defined in Equation 2-2. Now by considering Figure 2-2 and using the area coordinates defined in Equation 2-2, we can define edge bases for triangular a element as

Equation 2-8
$$\overline{\zeta_{ij}^e} = l_{ij}\left(L_i^e \nabla L_j^e - L_j^e \nabla L_i^e\right) \qquad i,j = 1,2,3$$

where $\overline{\zeta_{ij}^e}$ denotes the basis function and l_{ij} is the length for the edge formed by nodes i and j of the triangle. $\overline{\zeta_{ij}^e}$ has a constant tangential component along the edge formed by nodes i and j of the triangle and has no tangential component along other edges. Moreover, L_i^e vanishes along the edge opposite to node i. Thus tangential continuity is preserved across inter-element boundaries, but normal continuity is not. The vector field inside the triangular element can be written as

Equation 2-9
$$\overline{E_e} = \sum_{i,j=1,i\neq j}^{3} E_{ij}^e \overline{\zeta_{ij}^e} = \sum_{k=1}^{3} E_k^e \overline{\zeta_k^e}$$

where $\overline{E_e}$ is the field inside the triangular element, E_{ij}^e denotes the tangential field along the edge formed by nodes i and j of the e^{th} triangle.

High order vector basis functions involve adding nodes at each edge and including the contribution of face elements to the approximating function.

2.3.2 Three-dimensions

The derivation of basis functions for tetrahedral elements follow the same pattern as that for triangular vector basis functions. Considering the tetrahedron shown in Figure 2-5, we have

Equation 2-10
$$\overline{\zeta_{ij}^e} = l_{ij}\left(L_i^e \nabla L_j^e - L_j^e \nabla L_i^e\right) \qquad i,j = 1,2,3,4$$

where again $\overline{\zeta_{ij}^e}$ denotes the basis function, l_{ij} is the length for the edge formed by nodes i and j of the tetrahedron, and L_i^e is the volume coordinate. The vector field inside a tetrahedron element can be written as

Equation 2-11
$$\overline{E_e} = \sum_{i,j=1,i\neq j}^{4} E_{ij}^e \overline{\zeta_{ij}^e} = \sum_{k=1}^{6} E_k^e \overline{\zeta_k^e}$$

where $\overline{E_e}$ is the field inside the tetrahedral element, E_{ij}^e denotes the average tangential field along the edge formed by nodes i and j of the e^{th} tetrahedron.

2.4 Hierarchal edge elements

A drawback of the interpolatory basis functions, that have been discussed up to now, is that when the order of the polynomial is increased, completely new basis functions have to be generated. It is possible to avoid this by considering a series of basis functions that do not depend on the order of the polynomial. This indeed has been achieved with hierarchal basis functions. When the basis functions of an element are a subset of the basis functions of any element of higher order, the elements are called hierarchal [18]. The advantage of hierarchal elements is that elements of different orders can be used in the same mesh.

The interpolatory and hierarchic concepts for 1-dimensional scalar elements are shown pictorially in Figure 2-7. In the interpolatory approximation method, as shown in part (a) of Figure 2-7, each time the order of the basis functions is increased or decreased, all the basis functions $(\zeta_1', \zeta_2', \zeta_3')$ need to be regenerated – the previous functions (ζ_1, ζ_2) can

not be reused. But when the hierarchical approximation method is used, as shown in part (b) of Figure 2-7, the previously existing basis functions , in this case $\zeta_1' = \zeta_1$ and $\zeta_2' = \zeta_2$, do not need to be regenerated.

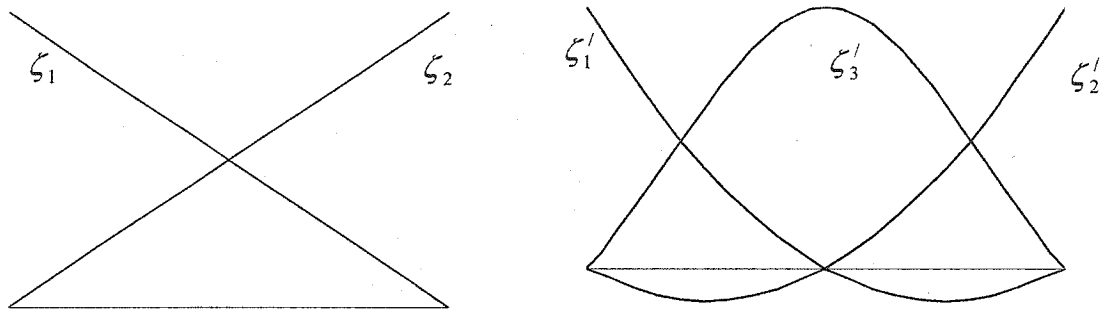

Order 1 Order 2

(a) Interpolatory approximation

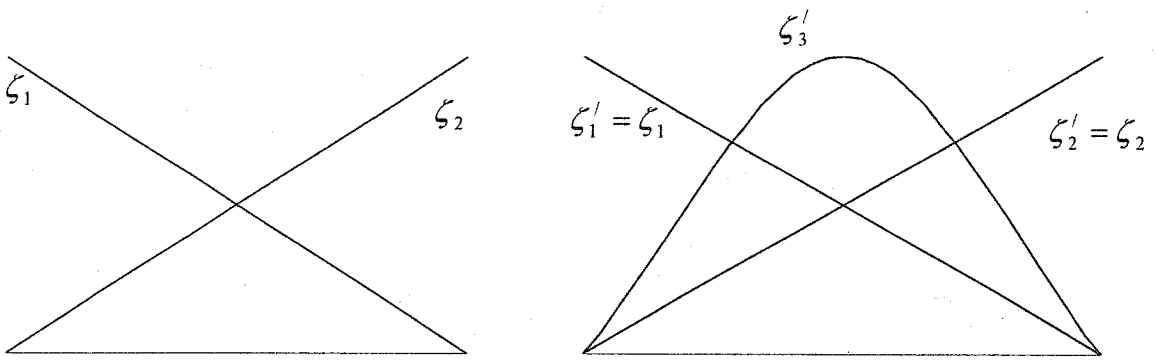

Order 1 Order 2

(b) Hierarchic approximation

Figure 2-7: Interpolatory vs Hierarchic basis functions

Hierarchal edge elements, like interpolatory edge elements, impose tangential continuity at the field interfaces, but not normal continuity. So, abrupt material interfaces for solving the curl-curl equation for $\overline{E}$ or $\overline{H}$ can be handled easily. It also eliminates spurious modes [18]. The finite element code that was used to generate results for this thesis uses hierarchal edge elements as presented by Webb [19].

2.5 Variational method

In FEM, the original boundary-value problem with an infinite number of degrees of freedom is converted into a problem with a finite number of degrees of freedom, or in other words, the solution of the whole system is approximated by a finite number of unknown coefficients. Then a set of algebric equations or a system of equations is obtained by applying the Ritz (variational) or Galerkin procedures, and finally, the solution of the boundary-value problem is achieved by solving the system of equations [8].

2.5.1 Ritz vs Galerkin method

The Ritz method, also known as the Rayleigh-Ritz method, is a variational method in which the boundary-value problem is formulated in terms of a variational expression referred to as a functional. The minimum of the functional corresponds to the governing differential equation under the given boundary conditions. The approximate solution is then obtained by finding the stationary point of the functional with respect to its variables.

Galerkin's method belongs to the family of weighted residual methods, which seek the solution by weighting the residual of the differential equation. In this method, the weighting function is selected to be the same as those used for the expansion of the approximate solution. This usually leads to a more accurate solution [8] and is, therefore, a popular approach in developing the finite element equations.

The variational method is one of the two methods often employed to formulate finite element solutions. There are several advantages associated with the variational method. The primary advantage is its solid foundation in physics and mathematics. Another advantage is that through the variational procedure one can clearly demonstrate the differences between the essential and natural conditions, which are difficult to comprehend for the beginner. Other advantages include convenience of description and elegance of the formulation. Because of these, the variational method was usually

preferred over Galerkin's method in the past [8].

However, the variational method has several disadvantages that makes it an unpopular choice now, particularly in electromagnetics. Unlike Galerkin's method, which starts directly with differential equations, the variational method starts from a variational formulation. Therefore, the applicability of the method depends directly on the availability of such a variational formulation. If a general procedure to derive the variational formulation for any given problem can be established, there would be no major obstacle, except for personal preference, to prevent from employing the variational method for the finite element formulation.

2.5.2 Formulation of system equation via Galerkin Method

A formulation employing the electric field $\overline{E}$ is presented for the solution of a general 3-D vector problem. A weak formulation [15] is derived through a Galerkin weighted residual procedure, and edge elements that impose tangential, but not necessarily normal continuity of the approximated field, are used for the presentation of the electric intensity and the discretization of the problem.

2.5.2.1 Derivation of Helmholtz equation

James C. Maxwell (1831-1879) published his electromagnetic field equations in 1864. He brought together previous experimental works and concepts of Gauss, Ampere and Faraday and his own knowledge of mathematics to present his analysis of electromagnetic fields [20]. Maxwell's equations form the basic for the theory of electromagnetic fields and waves.

For time-varying fields, the differential forms of the two curl equations are

Equation 2-12 $$\nabla \times \overline{E} = -j\omega \overline{B}$$

Equation 2-13 $$\nabla \times \overline{H} = \overline{J} + j\omega \overline{D}$$

where $\overline{E}$ and $\overline{H}$ are the electric and magnetic field intensities, $\overline{D}$ and $\overline{B}$ are the electric and magnetic flux densities, $\overline{J}$ is the current density and ϖ is the angular frequency of the field. Electric and magnetic flux densities $\overline{D}$ and $\overline{B}$, and current density $\overline{J}$ can be defined as

Equation 2-14 $$\overline{B} = \overline{\overline{\mu}}\,\overline{H}$$

Equation 2-15 $$\overline{D} = \overline{\overline{\varepsilon}}'\,\overline{E}$$

Equation 2-16 $$\overline{J} = \overline{\overline{\sigma}}\,\overline{E}$$

where $\overline{\overline{\mu}}$ is the permeability matrix (which could be complex), $\overline{\overline{\varepsilon}}'$ is the permittivity matrix, and $\overline{\overline{\sigma}}$ is the conductivity matrix of the medium. By substituting Equation 2-14 into Equation 2-12, the curl of the electric field $\overline{E}$ can be re-written as

Equation 2-17 $$\nabla \times \overline{E} = -j\varpi \overline{\overline{\mu}}\,\overline{H}$$

Similarly, the curl of the magnetic field $\overline{H}$ can be re-written using Equation 2-15 and Equation 2-16 as

Equation 2-18 $$\nabla \times \overline{H} = j\varpi \overline{\overline{\varepsilon}}\,\overline{E}$$

where

Equation 2-19 $$\overline{\overline{\varepsilon}} = \overline{\overline{\varepsilon}}' + \frac{\overline{\overline{\sigma}}}{j\varpi}$$

Taking the curl of Equation 2-17 and substituting in the expression for the curl of $\overline{H}$ from Equation 2-18, a second order differential equation known as the vector Helmholtz, or curl-curl, equation is obtained:

Equation 2-20 $$\nabla \times \frac{-1}{j\varpi} \frac{1}{\overline{\overline{\mu}}} \nabla \times \overline{E} - j\varpi \overline{\overline{\varepsilon}}\,\overline{E} = 0$$

The permittivity $\overline{\overline{\varepsilon}}$ and the permeability $\overline{\overline{\mu}}$ in Equation 2-20 can be written as

Equation 2-21 $$\overline{\overline{\varepsilon}} = \varepsilon_0 \overline{\overline{\varepsilon_r}}$$

Equation 2-22 $$\overline{\overline{\mu}} = \mu_0 \overline{\overline{\mu_r}}$$

where ε_0 and μ_0 are the permittivity and permeability of the free space, and ε_r and μ_r are the relative permittivity and permeability of the material. Then Equation 2-20 can be re-written as:

Equation 2-23 $$\nabla \times \frac{1}{\overline{\overline{\mu_r}}} \nabla \times \overline{E} - k_0 \overline{\overline{\varepsilon_r}}\, \overline{E} = 0$$

where the free space wave number $k_0 = \omega\sqrt{\varepsilon_0 \mu_0}$.

2.5.2.2 Boundary conditions

A unique solution can be obtained only after the specification of boundary conditions which constrain the values of the field at the boundaries of the domain. These boundary conditions, also referred to as boundary constraints, come in various forms. Three types of boundary conditions were encountered in this thesis:

The *Neumann boundary condition* constrains the tangential part of the curl of the electric field on the surface, and can be stated as

Equation 2-24 $$\hat{n} \times \nabla \times \overline{E} = 0 \qquad \text{on } S$$

where $\hat{n}$ denotes the outgoing unit normal vector of the domain boundary, as illustrated in Figure 2-8.

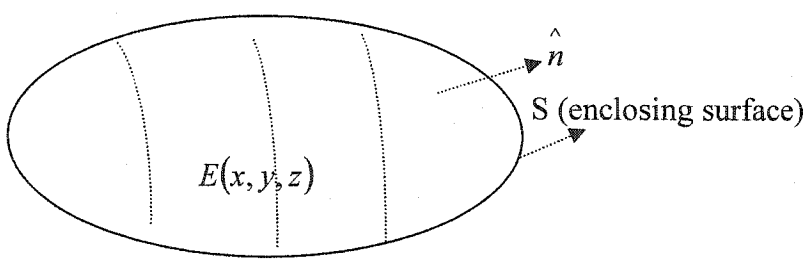

Figure 2-8: Surface encloser [15]

Equation 2-24 can be re-written as

Equation 2-25 $\hat{n} \times \overline{H} = 0$

which physically represents a magnetic wall [21], also called perfect magnetic conductor (PMC).

The *Dirichlet boundary condition* constraints the tangential component of the field on the surface, and can be stated as

Equation 2-26 $\hat{n} \times \overline{E} = E_0$ on S

If $E_0 = 0$, the surface physically represents an electric wall, which can be denoted as a short circuit or a perfect electric conductor (PEC). If $E_0 \neq 0$, the surface excites the problem. However, in this thesis $E_0 = 0$ is assumed.

2.5.2.3 Port Boundary Condition

To model microwave circuits, it is required that the sources at the input ports excite the circuit. The source modeling issue is critical since it provides the input boundary condition for the problem. A small error in the source modeling could lead to large errors in the 3-D simulation of the circuit parameters [15].

Consider the q^{th}-port junction in Figure 2-9

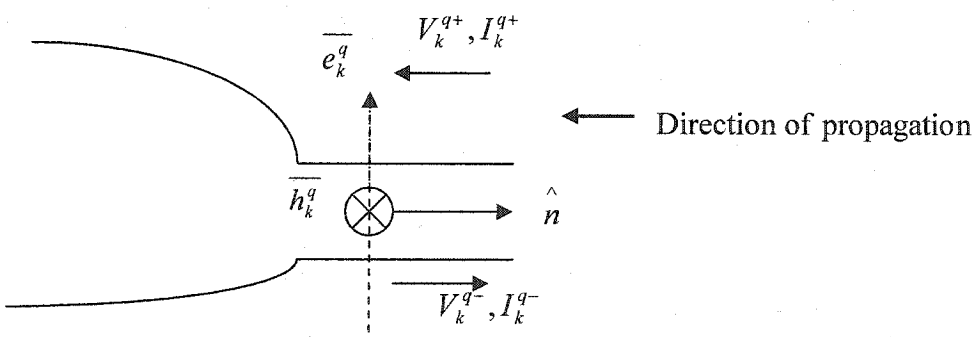

Figure 2-9: A general q^{th} port of a waveguide junction [21]

In general, a port can support multiple modes of propagation for a particular frequency. For each mode k, incident and reflected waves move towards and away, respectively, from the port. However, a practical device is usually designed to allow only dominant mode propagation and will be treated as such in the formulations in this thesis.

For the k^{th} mode, let the transverse electric and magnetic fields for the incident wave be $\overline{e_k^q}$ and $\overline{h_k^q}$ respectively, and assume only one mode to be present. If $\overline{E_t}$ and $\overline{H_t}$ are the tangential electric and magnetic fields at port q, then

Equation 2-27 $$\overline{E_t} = f^+ \overline{e_k^q} + f^- \overline{e_k^q} = \overline{e_k^q}\left(f^+ + f^-\right)$$

Equation 2-28 $$\overline{H_t} = f^+ \overline{h_k^q} - f^- \overline{h_k^q} = \overline{h_k^q}\left(f^+ - f^-\right)$$

where f^+ and f^- are multipliers that do not vary with position over the waveguide cross-section. If V_k^q and I_k^q are terminal voltage and current, respectively, of port q for the k^{th}-mode, then the tangential electric and magnetic fields $\overline{E_t}$ and $\overline{H_t}$ at port q can be written as

Equation 2-29 $$\overline{E_t} = k_1 V_k^q \overline{e_k^q}$$

Equation 2-30 $$\overline{H_t} = k_2 I_k^q \overline{h_k^q}$$

where k_1 and k_2 are unknowns. Combining Equation 2-27 with Equation 2-29, and Equation 2-28 with Equation 2-30 gives give

Equation 2-31 $$V_k^q = \frac{f^+ + f^-}{k_1}$$

Equation 2-32 $$I_k^q = \frac{f^+ - f^-}{k_2}$$

From the definition of power in circuit theory and electromagnetic theory,

Equation 2-33
$$P_{real} = \frac{1}{2}\mathrm{Re}\left(V_k^q I_k^{q*}\right)$$

Equation 2-34
$$P_{real} = \frac{1}{2}\mathrm{Re}\int \overline{E_t} \times \overline{H_t}^* \cdot \left(-\hat{n}\right) ds$$

where P_{real} is the real power flow into the port q. Equating Equation 2-33 and Equation 2-34 and using Equation 2-27, Equation 2-28, Equation 2-31, and Equation 2-32 gives

Equation 2-35
$$k_1 k_2^* = \frac{1}{\int_s e_k^q \times h_k^{q*} \cdot \left(-\hat{n}\right) ds}$$

Normalization of e_k^q and h_k^q of Equation 2-35 corresponds to unit power flow into the device. So,

Equation 2-36
$$k_1 k_2^* = 1$$

Now let us assume that voltage and current are *normalized*, i.e., the characteristic impedance, Z_0, is unity:

Equation 2-37
$$Z_0 = \frac{V_k^{q+}}{I_k^{q+}} = 1$$

We can use this to obtain one more condition for k_1 and k_2. For an incident wave at port p, the tangential electric field $\overline{E_t}$ and the tangential magnetic field $\overline{H_t}$ of Equation 2-27 and Equation 2-28, respectively, can be re-written using Equation 2-31 and Equation 2-32 as

Equation 2-38
$$\overline{E_t} = f^+ \overline{e_k^q} = k_1 V_k^{q+} \overline{e_k^q}$$

Equation 2-39
$$\overline{H_t} = f^+ \overline{h_k^q} = k_2 I_k^{q+} \overline{h_k^q}$$

where V_k^{q+} and I_k^{q+} are the voltage and current of the wave traveling towards the port q. Hence:

Equation 2-40

$$\frac{k_1 V_k^{q+}}{k_2 I_k^{q+}} = \frac{f^+}{f^+} = 1$$

So,

Equation 2-41

$$Z_0 = \frac{V_k^{q+}}{I_k^{q+}} = \frac{k_2}{k_1}$$

Similarly, for the wave traveling out of the port q

Equation 2-42

$$Z_0 = -\frac{V_k^{q-}}{I_k^{q-}} = \frac{k_2}{k_1}$$

From Equation 2-36, Equation 2-37, Equation 2-41, and Equation 2-42

Equation 2-43

$$k_1 = k_2 = 1$$

Thus the tangential electric field $\overline{E_t}$ and the tangential magnetic field $\overline{H_t}$ for an incident wave at port q for mode k, from Equation 2-38 and Equation 2-39, can be re-written as

Equation 2-44

$$\overline{E_t} = V_k^{q+} \overline{e_k^q}$$

Equation 2-45

$$\overline{H_t} = I_k^{q+} \overline{h_k^q}$$

Similarly, for the reflected wave,

Equation 2-46

$$\overline{E_t} = V_k^{q-} \overline{e_k^q}$$

Equation 2-47

$$\overline{H_t} = I_k^{q-} \overline{h_k^q}$$

When both the incident and reflected waves are present, total tangential fields are the summation of the tangential field components of the incident and reflected waves. Thus the total tangential electric field $\overline{E_t}$ at port q for mode k is the summation of Equation 2-44 and Equation 2-46.

Equation 2-48

$$\overline{E_t} = V_k^q \overline{e_k^q}$$

where the normalized voltage V_k^q at port q for mode k is defined by

Equation 2-49

$$V_k^q = V_k^{q+} + V_k^{q-}$$

Similarly, the total tangential magnetic field $\overline{H_t}$ at port q for mode k can be written from Equation 2-45 and Equation 2-47 as

Equation 2-50 $$\overline{H_t} = I_k^q \overline{h_k^q}$$

where the normalized current I_k^q at port q for mode k are defined by

Equation 2-51 $$I_k^q = I_k^{q+} + I_k^{q-}$$

The incident and reflected current I_k^{q+} and I_k^{q-} at port q for mode k of Equation 2-41 and Equation 2-42 can be written using Equation 2-43 in terms of incident and reflected voltage V_k^{q+} and V_k^{q-} as

Equation 2-52 $$I_k^{q+} = V_k^{q+}$$

Equation 2-53 $$I_k^{q-} = -V_k^{q-}$$

The total current I_k^q at port q for mode k is the summation of incident and reflected currents of Equation 2-52 and Equation 2-53:

Equation 2-54 $$I_k^q = V_k^{q+} - V_k^{q-}$$

Equation 2-54 can be re-written in terms of total and incident voltages V_k^q and V_k^{q+} as:

Equation 2-55 $$I_k^q = 2V_k^{q+} - V_k^q$$

Suppose, a unit incident wave is imposed on port p for the dominant mode $k = 0$, with all the other ports being matched. The incident voltages then become:

Equation 2-56 $$V_k^{q+} = \delta_{pq}\delta_{k0}$$

where δ_{pq} is the Kroenecker delta function. For $p = q, V_k^{q+}$ is a unit excitation for the dominant mode and is unity for mode 0 and zero for all other modes. Now, Equation 2-55 can be re-written as

Equation 2-57 $$I_k^q = 2\delta_{pq}\delta_{k0} - V_k^q$$

Let $\overline{E}_0^p$, and $\overline{H}_0^p$ be the total electric and magnetic field and $\overline{E}_{0t}^p$, and $\overline{H}_{0t}^p$ be the total

tangential electric and magnetic field in the device due to dominant mode excitation at port p. Using Equation 2-50 on port q total tangential component of electric field $\overline{E}_{0t}^{p}$ becomes

Equation 2-58 $$\overline{H_{ot}^{p}} = \sum_{l=0}^{\infty} I_l^q \overline{h_l^q}$$

Where the summation allows for an infinite number of modes on port q. Substituting Equation 2-47 for the current into Equation 2-58, the total tangential magnetic field becomes

Equation 2-59 $$\overline{H}_{0t}^{p} = \sum_{l=0}^{\infty} \left(2\delta_{pq}\delta_{0l} - V_l^q\right)\overline{h}_l^q$$

If port q is not the excited port$(p \neq q)$, the incident voltage is at port p, thus the first term of Equation 2-59 becomes zero for all modes.

When port p is excited with the dominant mode, the total tangential electric field $\overline{E_{0t}^{p}}$ on port q is the sum of all modal tangential electric fields. Then using Equation 2-48 the total tangential electric field becomes

Equation 2-60 $$\overline{E_{ot}^{p}} = \sum_{l=0}^{\infty} V_l^q \overline{e_l^q}$$

By taking the cross product with $\overline{h}_k^q$ and integrating over port q, Equation 2-60 becomes

Equation 2-61 $$\int_q \overline{E_{ot}^{p}} \times \overline{h_k^q}.\overline{ds} = \sum_{l=0}^{\infty} V_l^q \int_q \overline{e_l^q} \times \overline{h_k^q}.\overline{ds}$$

where $\overline{e_l^q}$ and $\overline{h_k^q}$ are normalized transverse electric and magnetic fields, respectively. The integral part on the right side of Equation 2-61 is evaluated to be the unit power flow into the port q.

Equation 2-62 $$\int_q \overline{e_l^q} \times \overline{h_k^q}.\overline{ds} = \delta_{lk}$$

Then Equation 2-61 can be re-written as

Equation 2-63

$$\int_q \overline{E_{ot}^p} \times \overline{h_k^q} . \overline{ds} = V_k^q$$

For dominant mode excitation at port p with modal voltages extracted, the k^{th} mode voltage at port q from electric field $\overline{E_0^p}$ can be written as

Equation 2-64

$$\gamma_k^q\left(\overline{E_0^p}\right) = \int_q \overline{E_o^p} \times \overline{h_k^q} . \overline{ds}$$

where $\gamma_k^q\left(\overline{E_0^p}\right)$ is a linear operator for extracting the k^{th} mode voltage. The total tangential magnetic field $\overline{H}_{0t}^p$ at port q, due to the dominant mode excitation at port p, of Equation 2-59 can be re-written using Equation 2-63 and Equation 2-64 as

Equation 2-65

$$\overline{H}_{0t}^p = 2\delta_{pq}\overline{h}_0^q - \sum_{l=0}^{\infty} \gamma_l^q\left(\overline{E}_0^p\right)\overline{h}_l^q$$

Equation 2-65 represents two things: (1) The first term represents the dominant-mode wave incident on port p; (2) the second term (summation) represents an absorbing boundary condition (ABC) for all the reflected, or outward going waves of the device.

A similar formulation for the reflected waves can be derived; however, assuming only incident waves has proven to be an adequately accurate approximation [21].

2.5.2.4 Galerkin weighted residual formulation

Suppose it is required to compute the electric field intensity $\overline{E}_0^p$ of an $N-$port microwave device where port p is excited with its dominant mode $(k=0)$ and all other ports are matched. The equation that governs the behavior of $\overline{E}_0^p$ in a microwave device is the Helmholtz equation given by Equation 2-23. As is the case with any differential equation, a unique solution can be obtained only after the specification of boundary conditions. These boundary conditions are expressed in as PMC (Equation 2-25), PEC (Equation 2-26), and port boundary condition (Equation 2-65), which are pictorially shown in Figure 2-10.

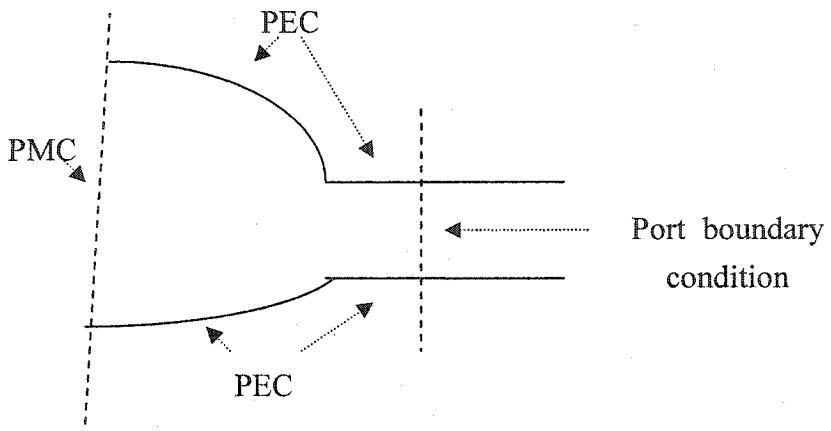

Figure 2-10: Boundary conditions [21]

To find the electric field $\overline{E}_0^p$ of the stated problem, with the above boundary conditions, terms are added to the usual weighted-residual formulation of the Helmholtz or curl-curl equation [22]. The weighted-residual can be defined as

Equation 2-66
$$B\left(\overline{E}_0^p, \overline{w}\right) = R\left(\overline{w}\right)$$

where B is the bilinear form given by [21]

Equation 2-67
$$B\left(\overline{E}_0^p, \overline{w}\right) = \frac{1}{jk_0\overline{\overline{\eta}}_0}\int_\Omega \left[\nabla\times\overline{E}_0^p . \frac{1}{\mu_r}\nabla\times\overline{w} - k_0^2\overline{E}_0^p . \overline{\overline{\varepsilon}}_r\,\overline{w}\right] d\Omega + \sum_{q=1}^{N}\sum_{l=0}^{\infty}\gamma_l^q\left(\overline{E}_0^p\right)\gamma_l^q\left(\overline{w}\right)$$

where $\overline{\overline{\eta}}_0$ is the intrinsic impedance of the free space. The residual $\overline{R}$ is given by the linear function

Equation 2-68
$$R\left(\overline{w}\right) = 2\gamma_0^p\left(\overline{w}\right)$$

2.5.2.5 Discretization with edge elements

The unknown in tetrahedral edge elements is the circulation of the vector field along the edges of the tetrahedron. The basis functions $\overline{\zeta_{ij}}$ for a typical edge e connecting vertices i and j of a tetrahedron edge element are given by Equation 2-10. The electric field is

approximated with edge elements which is similar to Equation 2-11, and can be given as

Equation 2-69
$$\overline{E}_0^p = \sum_{n=1}^{i} \overline{E}_{0i}^p \overline{\zeta}_i$$

where $\overline{\zeta}_i$ are the basis functions of edge elements, n is the number of edges of the finite element mesh, and the terms $\overline{E}_{0i}^p$ are the circulations of the electric field along the edges of the mesh.

If the vector basis functions $\overline{\zeta}_i$ of edge elements are used as weighting functions, $\overline{W}_i = \overline{\zeta}_i$, then Equation 2-66 can be discretized as

Equation 2-70
$$\left[\frac{1}{jk_0\eta_0}\{[S]+[T]\}+[U]\right]\left[\overline{E}_0^p\right]=[b]$$

where $[S]$, $[T]$, $[U]$, and $[b]$ are the matrices given as

Equation 2-71
$$S_{ij} = \int_{\Omega} \frac{1}{\mu_r}\left(\nabla \times \overline{W}_i\right)\left(\nabla \times \overline{W}_j\right)d\Omega$$

Equation 2-72
$$T_{ij} = -k_0^2 \varepsilon_r \int_{\Omega} \overline{W}_i . \overline{W}_j d\Omega$$

Equation 2-73
$$U_{ij} = \sum_{q=1}^{N}\sum_{l=0}^{\infty} \gamma_l^q\left(\overline{W}_i\right)\gamma_l^q\left(\overline{W}_j\right)$$

Equation 2-74
$$b_i = 2\gamma_0^p\left(\overline{W}_i\right)$$

The solution to Equation 2-70 can be obtained with iterative preconditioned conjugate gradient technique. Conjugate gradient techniques are often regarded as among the most powerful techniques for solving many types of linear algebra problems that strike a balance between the simplicity of the steepest descent method and the speed of the Newton-Raphson method [23]. These methods are typically simple to implement, especially for the quadratic case. In addition, storage requirements are far less than the quasi-Newton methods. In practice, these methods exhibit very fast convergence due to the orthogonalization of the descent direction. Possibilities for preconditioning exist, further improving convergence.

3 The Anisotropic Perfectly Matched Layer

3.1 Introduction

One of the most important aspects of finite-difference and finite element implementations is the truncation of the computational volume. An ideal truncation scheme must ensure that outgoing waves are not reflected backward at the mesh truncation surface. Among the truncation schemes used with the FEM, presently the most powerful formulation is the Perfectly Matched Layer (PML) approach. In 1994, Berenger [12] introduced the concept of PMLs in the FDTD computation. Since then, there has been extensive research to address various aspects of this promising approach. Among them, the anisotropic PML approach [3] is the most suitable for FEM implementation due to the fact that it accomplishes the PML property using an anisotropic material tensor, not by splitting the Maxwell equations [3]. Implementation of the anisotropic PML approach is straight forward, especially in the frequency domain. In fact, implementing the anisotropic PML approach in an existing FEM code requires no modification at all, provided that the code permits diagonally anisotropic material. A brief derivation of the anisotropic PML, the behaviour of waves in the PML medium, and the performance parameters of the PML are presented below by considering the simple plane wave incidence problem shown in Figure 3-1.

3.2 Waves in Anisotropic media

As shown in Figure 3-1, a uniform plane wave in air (μ_0, ε_0) of frequency f is incident obliquely at an angle of incidence θ_i on a plane interface at $z = 0$ with a medium having permeability and permittivity $\overline{\overline{\mu}}$ and $\overline{\overline{\varepsilon}}$, respectively.

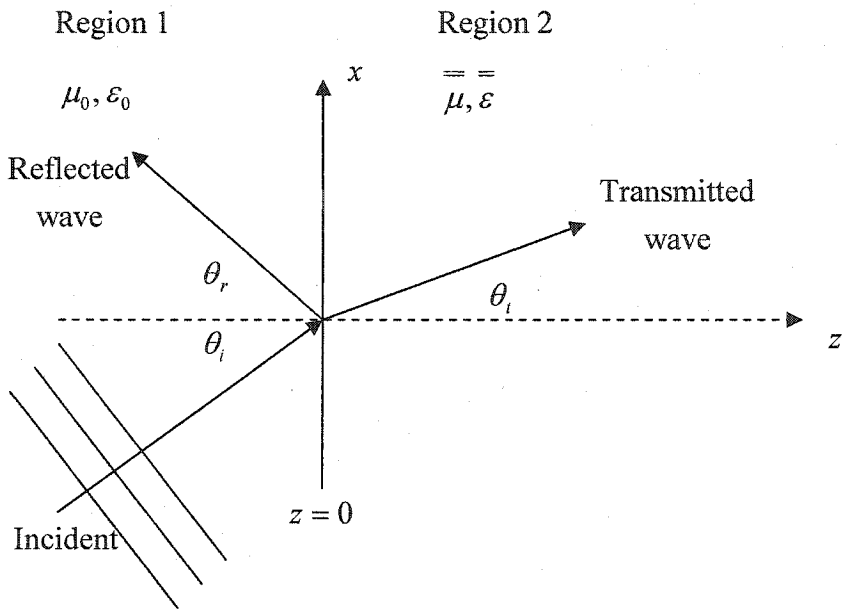

Figure 3-1: A plane wave incident upon a half-space anisotropic media [13]

The time-harmonic form of Maxwell's equations in Region 2 can be written as

Equation 3-1 $$\overline{\nabla}.\overline{\overline{\varepsilon}}\,\overline{E} = 0$$

Equation 3-2 $$\overline{\nabla}.\overline{\overline{\mu}}\,\overline{H} = 0$$

Equation 3-3 $$\overline{\nabla} \times \overline{E} = -j\omega\overline{\overline{\mu}}\,\overline{H}$$

Equation 3-4 $$\overline{\nabla} \times \overline{H} = j\omega\overline{\overline{\varepsilon}}\,\overline{E}$$

Parameters $\overline{\overline{\mu}}$ and $\overline{\overline{\varepsilon}}$ are assumed to be complex diagonal tensors in the same coordinate system, of the form

Equation 3-5

$$\overline{\overline{\mu}} = \mu_0 \begin{pmatrix} \mu_x + \frac{\sigma_M^x}{j\omega} & 0 & 0 \\ 0 & \mu_y + \frac{\sigma_M^y}{j\omega} & 0 \\ 0 & 0 & \mu_z + \frac{\sigma_M^z}{j\omega} \end{pmatrix}$$

Equation 3-6

$$\overline{\overline{\varepsilon}} = \varepsilon_0 \begin{pmatrix} \varepsilon_x + \frac{\sigma_E^x}{j\omega} & 0 & 0 \\ 0 & \varepsilon_y + \frac{\sigma_E^y}{j\omega} & 0 \\ 0 & 0 & \varepsilon_z + \frac{\sigma_E^z}{j\omega} \end{pmatrix}$$

where $\overline{\overline{\sigma}}_M$ and $\overline{\overline{\sigma}}_E$ are the magnetic and electric conductivities, respectively. When an electromagnetic wave traveling in one medium impinges on another medium with a different intrinsic impedance, it experiences a reflection [24]. The material properties of medium 2 (PML) can be chosen such that the interface between medium 2 and medium 1 (free space) is perfectly reflectionless. For a reflectionless interface, the intrinsic impedance of medium 1 has to be same as the intrinsic impedance of medium 2. To match the intrinsic impedances the following condition is required

Equation 3-7

$$\frac{\overline{\overline{\varepsilon}}}{\varepsilon_0} = \frac{\overline{\overline{\mu}}}{\mu_0}$$

Thus the material properties for medium 2 can be written as

Equation 3-8

$$\overline{\overline{\mu}} = \mu_0 \overline{\overline{\Lambda}} = \mu_0 \begin{pmatrix} a & 0 & 0 \\ 0 & b & 0 \\ 0 & 0 & c \end{pmatrix}$$

Equation 3-9

$$\overline{\overline{\varepsilon}} = \varepsilon_0 \overline{\overline{\Lambda}} = \varepsilon_0 \begin{pmatrix} a & 0 & 0 \\ 0 & b & 0 \\ 0 & 0 & c \end{pmatrix}$$

where $a, b,$ and c are, in general, complex. Consequently, in the PML medium, the time-harmonic form of Maxwell's equations of Equation 3-1, Equation 3-2, Equation 3-3, and

Equation 3-4 reduce to

Equation 3-10 $$\bar{\nabla}.\bar{\bar{\Lambda}}\bar{E} = 0$$

Equation 3-11 $$\bar{\nabla}.\bar{\bar{\Lambda}}\bar{H} = 0$$

Equation 3-12 $$\bar{\nabla} \times \bar{E} = -j\omega\mu_0 \bar{\bar{\Lambda}}\bar{H}$$

Equation 3-13 $$\bar{\nabla} \times \bar{H} = j\omega\varepsilon_0 \bar{\bar{\Lambda}}\bar{E}$$

The phasor electric field of a uniform plane wave along an arbitrary direction has the general form of [24]

Equation 3-14 $$\bar{E}(x,y,z) = \bar{E}_0 e^{-jk_x x - jk_y y - jk_z z}$$

where ω is the angular frequency of the wave. Wave number vector $\bar{k}$ is defined as

Equation 3-15 $$\bar{k} = \hat{a}_x k_x + \hat{a}_y k_y + \hat{a}_z k_z$$

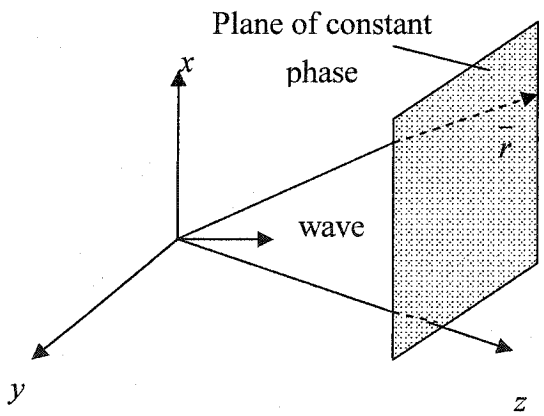

Figure 3-2: Radius vector $\bar{r}$ and wave normal to a phase front of a uniform plane wave [24]

and a radius vector $\bar{r}$ from the origin as shown in Figure 3-2 is defined as

Equation 3-16 $$\bar{r} = \hat{a}_x x + \hat{a}_y y + \hat{a}_z z$$

Then Equation 3-14 can be completely written as

Equation 3-17 $$\overline{E}(\overline{r}) = \overline{E}_0 e^{-j\overline{k}.\overline{r}}$$

where $\overline{E}_0$ is a constant vector. Similarly the expression for the magnetic field can be written as

Equation 3-18 $$\overline{H}(\overline{r}) = \overline{H}_0 e^{-j\overline{k}.\overline{r}}$$

where $\overline{H}_0$ is a constant vector. By substituting Equation 3-17 into Equation 3-10

$$\overline{\nabla}.\overline{\overline{\Lambda}}\overline{E}_0 e^{-j\overline{k}.\overline{r}} = 0$$

$$\Rightarrow \left(\frac{\partial}{\partial x}\hat{a}_x + \frac{\partial}{\partial y}\hat{a}_y + \frac{\partial}{\partial z}\hat{a}_z\right).\overline{\overline{\Lambda}}\left(E_{0x}\hat{a}_x + E_{0y}\hat{a}_y + E_{0z}\hat{a}_z\right)e^{-j\overline{k}.\overline{r}} = 0$$

But $\overline{k}.\overline{r} = xk_x + yk_y + zk_z$

then

$$\left(k_x\hat{a}_x + k_y\hat{a}_y + k_z\hat{a}_z\right).\overline{\overline{\Lambda}}\left(E_{0x}\hat{a}_x + E_{0y}\hat{a}_y + E_{0z}\hat{a}_z\right) = 0$$

So, Equation 3-10 becomes

Equation 3-19 $$\overline{k}.\overline{\overline{\Lambda}}\overline{E}_0 = 0$$

Similarly, by substituting

Equation 3-18 into Equation 3-11

Equation 3-20 $$\overline{k}.\overline{\overline{\Lambda}}\overline{H}_0 = 0$$

For the vector curl equation of the electric field, Equation 3-17 and Equation 3-18 are substituted into Equation 3-12:

$$\overline{\nabla} \times \overline{E}_0 e^{-j\overline{k}.\overline{r}} = -j\omega\mu_0 \overline{\overline{\Lambda}}\overline{H}_0 e^{-j\overline{k}.\overline{r}}$$

which can be simplified to

Equation 3-21 $$\bar{k} \times \bar{E}_0 = \omega \mu_0 \bar{\bar{\Lambda}} \bar{H}_0$$

Similarly, Equation 3-13 can be re-written as

Equation 3-22 $$\bar{k} \times \bar{H}_0 = -\omega \varepsilon_0 \bar{\bar{\Lambda}} \bar{E}_0$$

The dispersion relation which determines the form of the propagation vector $\bar{k}$ can be determined easily using the following variable transforms [13]

Equation 3-23 $$\bar{E}_0' = \left(\bar{\bar{\Lambda}}\right)^{\frac{1}{2}} \bar{E}_0$$

Equation 3-24 $$\bar{H}_0' = \left(\bar{\bar{\Lambda}}\right)^{\frac{1}{2}} \bar{H}_0$$

Equation 3-25 $$\bar{k}' = \frac{1}{\sqrt{abc}} \left(\bar{\bar{\Lambda}}\right)^{\frac{1}{2}} \bar{k}$$

Applying the transformations of Equation 3-23 and Equation 3-25 to Equation 3-19 results in:

$$\bar{k}.\bar{\bar{\Lambda}}\bar{E}_0 \doteq 0$$

$$\Rightarrow \sqrt{abc}\left(\bar{\bar{\Lambda}}\right)^{-\frac{1}{2}} \bar{k}'.\bar{\bar{\Lambda}}\left(\bar{\bar{\Lambda}}\right)^{-\frac{1}{2}} \bar{E}_0' = 0$$

$$\Rightarrow \sqrt{abc}\begin{pmatrix} \frac{1}{\sqrt{a}} & 0 & 0 \\ 0 & \frac{1}{\sqrt{b}} & 0 \\ 0 & 0 & \frac{1}{\sqrt{c}} \end{pmatrix}\left(k_x' \hat{a}_x + k_y' \hat{a}_y + k_z' \hat{a}_z\right).\begin{pmatrix} \sqrt{a} & 0 & 0 \\ 0 & \sqrt{b} & 0 \\ 0 & 0 & \sqrt{c} \end{pmatrix}\left(E_{0x}' \hat{a}_x + E_{0y}' \hat{a}_y + E_{0z}' \hat{a}_z\right) = 0$$

$$\Rightarrow \sqrt{abc}\left(k_x' \hat{a}_x + k_y' \hat{a}_y + k_z' \hat{a}_z\right).\left(E_{0x}' \hat{a}_x + E_{0y}' \hat{a}_y + E_{0z}' \hat{a}_z\right) = 0$$

So, in terms of the transformation variables of Equation 3-23 and Equation 3-25, Equation 3-19 can be written as

Equation 3-26 $$\bar{k}'.\bar{E}_0' = 0$$

Similarly, using the transformations of Equation 3-23 and Equation 3-24, Equation 3-20 can be written as

Equation 3-27 $$\bar{k}'.\bar{H}_0' = 0$$

For the curl equation, by applying the transformations of Equation 3-23, Equation 3-24, and Equation 3-25 to Equation 3-21 results in:

$$\bar{k} \times \bar{E}_0 = \omega\mu_0 \bar{\bar{\Lambda}} \bar{H}_0$$

$$\Rightarrow \left(\sqrt{abc} \left(\bar{\bar{\Lambda}}\right)^{\frac{-1}{2}} \bar{k}' \right) \times \left(\left(\bar{\bar{\Lambda}}\right)^{\frac{-1}{2}} \bar{E}_0' \right) = \omega\mu_0 \left(\bar{\bar{\Lambda}}\right)^{\frac{1}{2}} \bar{H}_0'$$

$$\Rightarrow \sqrt{abc} \begin{pmatrix} \frac{1}{\sqrt{a}} & 0 & 0 \\ 0 & \frac{1}{\sqrt{b}} & 0 \\ 0 & 0 & \frac{1}{\sqrt{c}} \end{pmatrix} \left(\bar{k}_x' \hat{a}_x + \bar{k}_y' \hat{a}_y + \bar{k}_z' \hat{a}_z \right) \times \begin{pmatrix} \frac{1}{\sqrt{a}} & 0 & 0 \\ 0 & \frac{1}{\sqrt{b}} & 0 \\ 0 & 0 & \frac{1}{\sqrt{c}} \end{pmatrix}$$

$$\left(\bar{E}_{0x}' \hat{a}_x + \bar{E}_{0y}' \hat{a}_y + \bar{E}_{0z}' \hat{a}_z \right) = \omega\mu_0 \left(\bar{\bar{\Lambda}}\right)^{\frac{1}{2}} \bar{H}_0'$$

$$\Rightarrow \left(\bar{\bar{\Lambda}}\right)^{\frac{1}{2}} \bar{k}' \times \bar{E}_0' = \omega\mu_0 \left(\bar{\bar{\Lambda}}\right)^{\frac{1}{2}} \bar{H}_0'$$

So, in terms of transformation variables of Equation 3-23, Equation 3-24, and Equation 3-25, Equation 3-21 can be written as

Equation 3-28 $$\bar{k}' \times \bar{E}_0' = \omega\mu_0 \bar{H}_0'$$

Similarly, in terms of the transformation variables of Equation 3-23, Equation 3-24 and Equation 3-25, Equation 3-22 can be written as

Equation 3-29 $$\bar{k}' \times \bar{H}_0' = -\omega\varepsilon_0 \bar{E}_0'$$

From Equation 3-28 and Equation 3-29 it is seen that $\bar{k}'$ is perpendicular to both $\bar{E}_0'$ and $\bar{H}_0'$. So, from Equation 3-28 and Equation 3-29

Equation 3-30

$$\left|\bar{k}'\right|\left|\bar{E}_0'\right|\hat{a}_H = \omega\mu_0\left|\bar{H}_0'\right|\hat{a}_H$$

Equation 3-31

$$-\left|\bar{k}'\right|\left|\bar{H}_0'\right|\hat{a}_E = -\omega\varepsilon_0\left|\bar{E}_0'\right|\hat{a}_E$$

Multiplying Equation 3-30 and Equation 3-31 results in

Equation 3-32

$$\left|\bar{k}'\right|^2 = \omega^2\varepsilon_0\mu_0 = k_0^2$$

Taking the dot product of $\bar{k}'$ and its transpose, and substituting Equation 3-32 into the resulting expression gives the dispersion relation as

$$\bar{k}'.\left[\bar{k}'\right]^T = \left[\frac{1}{\sqrt{abc}}\left(\bar{\bar{\Lambda}}\right)^{\frac{1}{2}}\bar{k}\right].\left[\frac{1}{\sqrt{abc}}\left(\bar{\bar{\Lambda}}\right)^{\frac{1}{2}}\bar{k}\right]^T$$

$$\Rightarrow k_0^2 = \frac{1}{abc}\begin{bmatrix}\sqrt{a}k_x & 0 & 0\\ 0 & \sqrt{b}k_y & 0\\ 0 & 0 & \sqrt{c}k_z\end{bmatrix}.\begin{bmatrix}\sqrt{a}k_x & 0 & 0\\ 0 & \sqrt{b}k_y & 0\\ 0 & 0 & \sqrt{c}k_z\end{bmatrix}^T$$

$$\Rightarrow k_0^2 = \frac{1}{abc}\left(ak_x^2 + bk_y^2 + ck_z^2\right)$$

which reduces to:

Equation 3-33

$$\frac{k_x^2}{bc} + \frac{k_y^2}{ca} + \frac{k_z^2}{ab} = k_0^2$$

Equation 3-33 is an equation of an ellipsoid whose solution can be written as

Equation 3-34

$$k_x = k_0\sqrt{bc}\sin\theta\cos\phi$$

Equation 3-35

$$k_y = k_0\sqrt{ac}\sin\theta\sin\phi$$

Equation 3-36

$$k_z = k_0\sqrt{ab}\cos\theta$$

As in Figure 3-1, the plane wave is restricted to the xz-plane $(\phi = 0)$, so Equation 3-34, Equation 3-35, and Equation 3-36 reduce to

Equation 3-37 $$k_x = k_0\sqrt{bc}\sin\theta$$

Equation 3-38 $$k_y = 0$$

Equation 3-39 $$k_z = k_0\sqrt{ab}\cos\theta$$

3.3 Reflection Coefficient

For a TE_y-polarized ($\bar{E}$ only has a y-component) wave, the incident electric field $\bar{E}_i(\bar{r})$ can be obtained from Equation 3-17 as

Equation 3-40 $$\bar{E}_i(\bar{r}) = E_{0y}\,\hat{a}_y\,e^{-j\bar{k}.\bar{r}}$$

where $\bar{k}$ for the incident wave of Figure 3-1 can be defined as

Equation 3-41 $$\bar{k} = k_0\sin\theta_i\,\hat{a}_x + k_0\cos\theta_i\,\hat{a}_z$$

and the position vector $\bar{r}$ is always defined by Equation 3-16. The electric field vector $\bar{E}_i(\bar{r})$ of Equation 3-40 can be re-written by substituting $\bar{k}$ and $\bar{r}$ by Equation 3-41 and Equation 3-16, respectively, as

Equation 3-42 $$\bar{E}_i(\bar{r}) = E_{0y}\,\hat{a}_y\,e^{-jk_0(\sin\theta_i x+\cos\theta_i z)}$$

The reflected electric field $\bar{E}_r(\bar{r})$ for TE_y-polarized wave of Figure 3-1 is given from Equation 3-17 as [24]

Equation 3-43 $$\bar{E}_r(\bar{r}) = R^{TE}E_{0y}\,\hat{a}_y\,e^{-j(\bar{k}_r.\bar{r})}$$

where R^{TE} is the reflection coefficient for the TE-mode, which is given by [15]:

Equation 3-44

$$R^{TE} = \frac{\cos\theta_i - \left(\sqrt{\frac{b}{a}}\right)\cos\theta_t}{\cos\theta_i + \left(\sqrt{\frac{b}{a}}\right)\cos\theta_t}$$

and the wave number vector $\bar{k}_r$ for the reflected wave of Figure 3-1 is defined as

Equation 3-45

$$\bar{k}_r = k_0 \sin\theta_r \hat{a}_x - k_0 \cos\theta_r \hat{a}_z$$

The reflected electric field vector $\bar{E}_r(\bar{r})$ of Equation 3-43 can be re-written by substituting $\bar{k}_r$ and $\bar{r}$ from Equation 3-45 and Equation 3-16 as

Equation 3-46

$$\bar{E}_r(\bar{r}) = R^{TE} E_{0y} \hat{a}_y e^{-jk_0(\sin\theta_r x - \cos\theta_r z)}$$

Similarly, for the transmitted electric field $\bar{E}_t(\bar{r})$ for TE_y-polarized wave of Figure 3-1 is given from Equation 3-17 as [24]

Equation 3-47

$$\bar{E}_t(\bar{r}) = T^{TE} E_{0y} \hat{a}_y e^{-j(\bar{k}_t \cdot \bar{r})}$$

where T^{TE} is the transmission coefficient for the TE-mode, which is given by

Equation 3-48

$$T^{TE} = 1 + R^{TE}$$

and the wave number vector $\bar{k}_t$ for the transmitted wave of Figure 3-1 is defined by Equation 3-37, Equation 3-38, and Equation 3-39. The transmitted electric field vector $\bar{E}_t(\bar{r})$ of Equation 3-47 can then be re-written by substituting the values of $\bar{k}_t$ and $\bar{r}$ as

Equation 3-49

$$\bar{E}_t(\bar{r}) = T^{TE} E_{0y} \hat{a}_y e^{-jk_0\left(\sqrt{bc}\sin\theta_t x + \sqrt{ab}\cos\theta_t z\right)}$$

The phase matching conditions at the interface are the Snell's laws of reflection and refraction [24], which are defined, respectively, as [15]

Equation 3-50 $$\sin\theta_i = \sin\theta_r$$

Equation 3-51 $$\sqrt{bc}\sin\theta_t = \sin\theta_i$$

In order to make the reflection coefficient R^{TE} of Equation 3-44 independent of the incidence angle θ_i, from Equation 3-51 it can be seen that this can be obtained by assigning $\sqrt{bc}=1$. So, from Equation 3-51 it follows that $\theta_i = \theta_t$. Reflection coefficient R^{TE} of Equation 3-44 can be re-written as

Equation 3-52 $$R^{TE} = \frac{1-\left(\sqrt{\frac{b}{a}}\right)}{1+\left(\sqrt{\frac{b}{a}}\right)}$$

The zero reflection condition, as required for the PML, is achieved by setting $a = b$. So, from Equation 3-8 and Equation 3-9

Equation 3-53 $$\overline{\overline{\Lambda}} = \frac{\overline{\overline{\mu}}}{\mu_0} = \frac{\overline{\overline{\varepsilon}}}{\varepsilon_0} = \begin{pmatrix} a & 0 & 0 \\ 0 & a & 0 \\ 0 & 0 & \frac{1}{a} \end{pmatrix}$$

which makes the PML perfectly reflectionless for any frequency, angle of incidence and polarization.

3.4 Material Properties of Anisotropic PML

The PML layer is characterized by the complex number $a = s' - js''$ as shown in Equation 3-53. The design of the anisotropic absorber, therefore, reduces to determining the values of s' and s''. For $s', s'' > 0$, the equation for the transmitted wave of Equation 3-49 can be re-written as

Equation 3-54 $$\overline{E}_t = E_{oy}\,\hat{a}_y\, e^{-k_0 s''\cos\theta_i z} e^{-jk_0\left(\sin\theta_i x + s'\cos\theta_i z\right)}$$

From Equation 3-54, it can be seen that the parameter s'' is crucial since it controls the

rate of decay of the transmitted wave in the PML medium [13]. If s'' is too small, field decay is insufficient to eliminate reflection. Too large a value of s'' leads to reflection since the mesh is insufficient to model the sudden jump in the material property [15]. Theoretically, s' has no effect on the absorbing capability of the PML material for plane waves, as it only affects the wavelength in the PML. Therefore, to reduce the discretization errors, small values of s' are preferred as larger values of s' result in larger discretization errors due to the fact that the fields inside the PML region change more drastically and the mesh loses the capability to model them correctly. However, the convergence of the iterative solver is slower when s' is smaller than s''. As a result, $s' = s''$ provides a good compromise [3] and is used for this thesis.

The main interest for the PML in this case is to use it to absorb the scattered field from an object (horn antenna) in free space. Thus, the PML material must totally surround the scatterer, and the outer surface of the PML must also be terminated in some way. For this work, the PML was terminated with a perfect electric conductor (PEC). The PML material is placed in the shape of a rectangular box as shown in Figure 3-3 to truncate the computational domain.

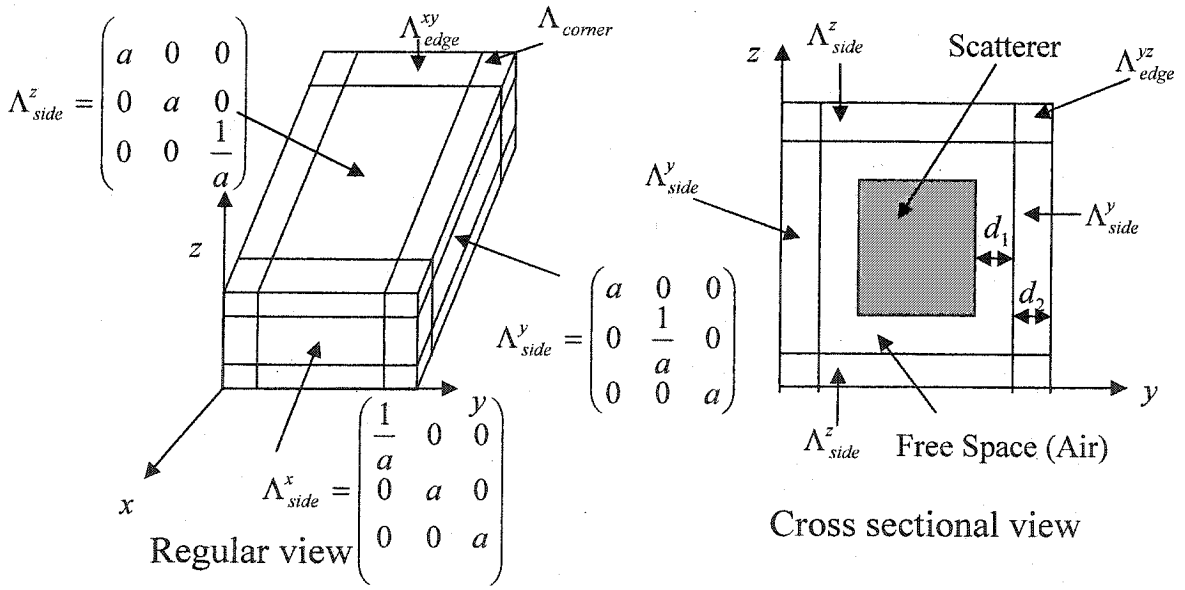

Figure 3-3: Geometry of the rectangular PML box surrounding the scatterer [3]

The material properties of the side regions of the PML box $\left(\Lambda^{i}_{side}, i = x, y, z\right)$ are similar to Equation 3-53, which is the material property of the sides parallel to both x and y axes as shown in Figure 3-3, where $a = s^{/} - js^{//}$ is an arbitrary complex number as was mentioned above. From electromagnetic theory, any choice would cause some diffracted field from the edges and corners. One possible approximation for the edge region is to choose the edge properties such that they are perfectly matched to the adjacent side regions when the edge/side interface is of infinite extent. By going through the analysis of a plane wave propagating through an infinite media interface, it can be seen that the material property of an edge is [3]

Equation 3-55 $$\Lambda^{mn}_{edge} = \Lambda^{m}_{side} \times \Lambda^{n}_{side} \qquad \text{where } m, n = x, y, z$$

A similar approach for the properties of the corner regions is to match the corner properties to the adjacent edges. By going through similar analysis, the material property of the corner region is [3]

Equation 3-56 $$\Lambda_{corner} = \Lambda^{x}_{side} \times \Lambda^{y}_{side} \times \Lambda^{z}_{side}$$

After obtaining the material property of each side, corner and edge, it is required to assign the thickness d_2 of each side of the PML box and the distance d_1 between the scatterer and the PML box as shown in Figure 3-3. The parameter d_1 should be kept as small as possible to reduce the computational cost. But if d_1 is too small, the PML is too close to the radiator (in this case the horn) which produces spherical waves, and the material property for the PML is assigned to absorb plane waves only. Spherical waves can be approximated as plane waves when the absorber is far from the radiator. If the radiator is too close to the PML, the solution accuracy also degrades due to discretization error [3]. So, for a better approximation, the PML should be as far away as possible from the radiator. Hence, there has to be a compromise between solution accuracy and computational cost.

The parameter d_2 has to be thick enough so that the transmitted wave can be absorbed fully before it reaches the outer boundary PEC wall. But to keep the computational cost

low, d_2 should be as small as possible. The product of s'' and d_2 determines the absorbing capability of the PML, so they have to be considered together [3].

4 Software

4.1 Introduction

To predict the radiation pattern and reflection coefficient of a horn using the FEM, programs such as FullWave [25], Excel [26], and P3D were used. As FullWave doesn't have the capability to truncate the computational domain for unbounded problems, modules for automating the PML (creating the PML, and assigning material property) were implemented. Programs for calculating the far field were also written and combined with existing programs.

4.2 Existing Components

To create the geometry of the PML Box and to generate the appropriate mesh for the model, the simulation software FullWave [25] was used. FullWave is a commercial program for solving scattering parameters of high frequency devices. FullWave has a good Graphical User Interface (GUI) for drawing microwave devices. It also has an Application Programmer Interface (API) to Visual Basic Application (VBA). Excel [26] embedded VBA was used to invoke FullWave to draw the geometry as well as to generate the mesh. Excel was used, because unlike Access or Word, it is a program well-suited for manipulating numerical data, transforming, plotting, etc. FullWave could not be used to solve for scattering parameters of unbounded scattering problems as it does not have the capability to truncate the computational domain (e.g. by a PML). Another limitation of FullWave is that it does not allow the user to change the order of the basis function (which is always the lowest order) or to use mixed hierarchal basis functions. A program named P3D, implemented in C++, was used to solve for the scattering parameters of the problem.

4.3 Automating the PML

To predict the radiation pattern of any type of radiator using the FEM, it is necessary to assign an artificial finite boundary that will represent the infinite free space beyond the FE mesh. In this thesis, a rectangular PML box is used. The same PML box can be used for different types and sizes of structures. With this in mind, programs for automating the process of setting up the rectangular PML box and its material properties were written and added to the existing P3D module.

4.3.1 PML Box

The rectangular PML box shown in Figure 4-1 is a complex structure of 27 different components. The reason for having so many components is that different material properties can be assigned to each component as it is required for the reflectionless Anisotropic PML absorber [3].

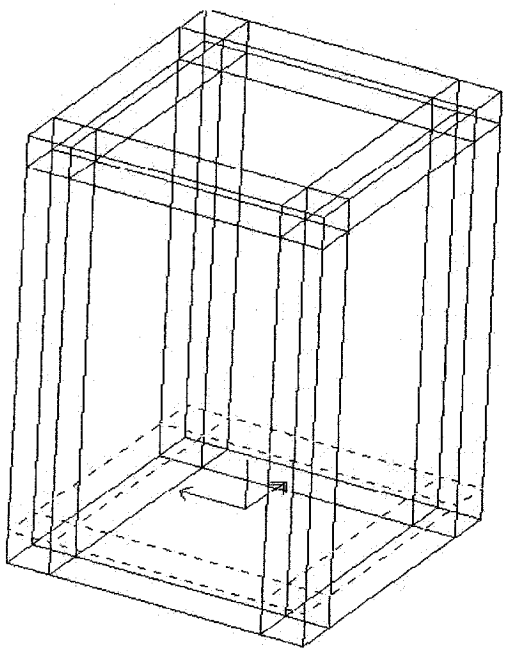

Figure 4-1: Rectangular PML box

To pass the geometric parameters of the PML box to FullWave, a subroutine called *automated_pml* was implemented in VBA and embedded in Excel.

The subroutine has the prototype

automated_pml(length, width, height, thickness)

The input parameters were the length, width and height of the central box which are parallel to the x, y and z axes, respectively, of the global coordinate frame. It also accepted the thickness of each of the outer most rectangular boxes as a parameter. Although it is possible to build the outer most boxes with different thicknesses, for simplicity this program drew all of them with the same thickness. By default, it drew the PML box centered at the origin. It can be changed easily by specifying the desired center of the PML box.

4.3.2 PML material properties

Using the theory presented in the previous chapter, material properties for each of the 27 components were assigned. A subroutine called *WritePML_Input(s1, s2, file_name)* was implemented using VBA to write a material data file that can be read by P3D. The *file_name* parameter passed the name of the material data file where the material property for each component of the PML box was saved. The parameters *s1* and *s2* were equivalent to s' and s'', respectively, which were defined in the previous chapter. A module called *code_pml* was implemented using C++, which calculated the appropriate reluctivity (the inverse of the permeability) and the permittivity of each component of the rectangular PML box as explained in the previous chapter, and saved them in the material data file. The ordering of the material property of each component of the PML box was the same as the order of the creation of the components. It will not contain the material properties of the components that are not part of the PML box. So, it was required to enter the material property for the components that were not part of the PML box manually at the end of the material data file. The material properties were symmetric tensors [27], so 6 complex values were needed for the *permittivity*, and 6 for the *reluctivity*..

If a material has permittivity (ε) and reluctivity (ν) as

Permittivity

$$\begin{matrix} \varepsilon_{11-Real} + j\varepsilon_{11-Imaginary} & \varepsilon_{12-Real} + j\varepsilon_{12-Imaginary} & \varepsilon_{13-Real} + j\varepsilon_{13-Imaginary} \\ \varepsilon_{21-Real} + j\varepsilon_{21-Imaginary} & \varepsilon_{22-Real} + j\varepsilon_{22-Imaginary} & \varepsilon_{23-Real} + j\varepsilon_{23-Imaginary} \\ \varepsilon_{31-Real} + j\varepsilon_{31-Imaginary} & \varepsilon_{32-Real} + j\varepsilon_{32-Imaginary} & \varepsilon_{33-Real} + j\varepsilon_{33-Imaginary} \end{matrix}$$

Reluctivity

$$\begin{matrix} \nu_{11-Real} + j\nu_{11-Imaginary} & \nu_{12-Real} + j\nu_{12-Imaginary} & \nu_{13-Real} + j\nu_{13-Imaginary} \\ \nu_{21-Real} + j\nu_{21-Imaginary} & \nu_{22-Real} + j\nu_{22-Imaginary} & \nu_{23-Real} + j\nu_{23-Imaginary} \\ \nu_{31-Real} + j\nu_{31-Imaginary} & \nu_{32-Real} + j\nu_{32-Imaginary} & \nu_{33-Real} + j\nu_{33-Imaginary} \end{matrix}$$

The material property of each component has the prototype

$\varepsilon_{11-Real}$	$\varepsilon_{11-Imaginary}$	$\nu_{11-Real}$	$\nu_{11-Imaginary}$
$\varepsilon_{21-Real}$	$\varepsilon_{21-Imaginary}$	$\nu_{21-Real}$	$\nu_{21-Imaginary}$
$\varepsilon_{22-Real}$	$\varepsilon_{22-Imaginary}$	$\nu_{22-Real}$	$\nu_{22-Imaginary}$
$\varepsilon_{31-Real}$	$\varepsilon_{31-Imaginary}$	$\nu_{31-Real}$	$\nu_{31-Imaginary}$
$\varepsilon_{32-Real}$	$\varepsilon_{32-Imaginary}$	$\nu_{32-Real}$	$\nu_{32-Imaginary}$
$\varepsilon_{33-Real}$	$\varepsilon_{33-Imaginary}$	$\nu_{33-Real}$	$\nu_{33-Imaginary}$

For example, air has the material property

1	0	1	0
0	0	0	0
1	0	1	0
0	0	0	0
0	0	0	0
1	0	1	0

4.4 Far Field

The radiation pattern of an antenna are three dimensional quantities involving the variation of the field or power as a function of the spherical coordinates θ and ϕ. Any field pattern can be presented in three-dimensional spherical coordinates, but for simplicity it is drawn by varying θ or ϕ, but not both [28]. Usually, the normalized field pattern is drawn. Dividing a field component by its maximum value, the normalized or relative field pattern, which is a dimensionless number with the maximum value of unity, is obtained. Thus the normalized field E_θ^n pattern for the θ component of the electric field E_θ is given by

Equation 4-1
$$E_\theta^n = \frac{E_\theta}{E_\theta^{\max}}$$

where $E_\theta^{\max}$ is the maximum θ component of the electric field.

The field around an antenna is divided into two principal regions, one near the antenna called the near field or Fresnel zone and one at a large distance called the far field or Fraunhofer zone [28].

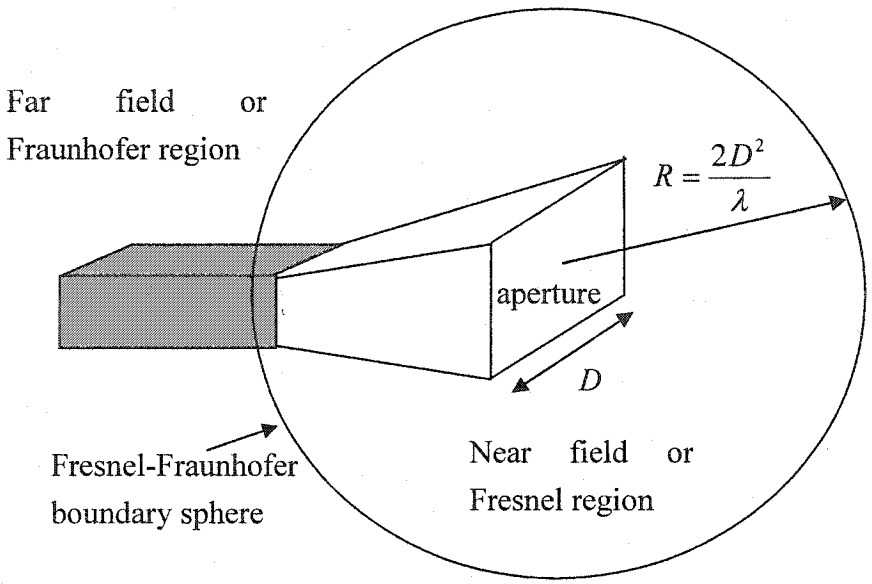

Figure 4-2: Fresnel region and Fraunhofer region [28]

Referring to Figure 4-2, the boundary between the two regions may be arbitrarily taken to be at a radius R as

Equation 4-2
$$R = \frac{2D^2}{\lambda}$$

where D is the maximum dimension of the antenna, and λ is the wavelength. The far-field region, or Fraunhofer region, is the region where spherical waves radiating from the aperture can be assumed to be plane waves with no variation in the plane transverse to the direction of travel. In the far field, the shape of the field pattern is independent of the distance. In the near or Fresnel region, the longitudinal component of the electric field may be significant and the power flow not entirely radial. In the near field, the shape of the field pattern depends, in general, on the distance.

In this thesis, far-field radiation patterns were evaluated. Using finite element method, the electric field in the near-field (aperture) of an antenna was computed. Then using Huygen's principle [2], the far-field at a distance r can be evaluated as

Equation 4-3
$$E_\theta = \frac{jk_0 e^{(-jk_0 r)}}{2\pi r}\left(f_x \cos\phi + f_y \sin\phi\right)$$

Equation 4-4

$$E_\phi = \frac{jk_0 e^{(-jk_0 r)}}{2\pi r}\cos\theta\left(f_y\cos\phi - f_x\sin\phi\right)$$

where k_0 is the free-space wave number, E_θ and E_ϕ are the magnitude of θ and ϕ components of electric field $\overline{E}$ at a distance r from the aperture, and f_x and f_y are defined over the aperture as

Equation 4-5

$$f_x = \int_{x'}\int_{y'} E_{ax}\left(x', y'\right) e^{\left\{jk\left(x'\sin\theta\cos\phi + y'\sin\theta\sin\phi\right)\right\}} dx'\,dy'$$

Equation 4-6

$$f_y = \int_{x'}\int_{y'} E_{ay}\left(x', y'\right) e^{\left\{jk\left(x'\sin\theta\cos\phi + y'\sin\theta\sin\phi\right)\right\}} dx'\,dy'$$

where E_{ax} and E_{ay} are the x and y components of electric field at the aperture.

To calculate the far field radiation pattern of a horn using Equation 4-3 and Equation 4-4, it is required to find the electric field at the aperture. To define an aperture, a plane perpendicular to the direction of radiation of the horn is selected which must be in front of the open-ended side of the horn. Moreover, this plane has to be inside the FE computational domain as the field only inside the computational domain is known. To find an aperture a function called *Find_tet(double z)* was implemented in C++ to create the data file *Tets_on_face.dat*, which contains all the tetrahedrons at the specified z coordinate. The $xy-$plane at the specified z coordinate behaves like the aperture of the radiator. To create a table (*temp_field.dat*) that contains electric field at the aperture a C++ function *Create_table(double z)* was implemented. The *temp_field.dat* file contains discretized x and y coordinates and the corresponding electric fields at those coordinates. A function called *evaluate(.....)* was implemented to evaluate Equation 4-5 and Equation 4-6. To perform the integrations of Equation 4-5 and Equation 4-6, Composite Simpson's rule [29] was implemented. To implement Equation 4-5 and Equation 4-6, they were rewritten in a general form as:

Equation 4-7

$$\int_a^b\left(\int_{c(x)}^{d(x)} f(x,y)dy\right)dx$$

First, Simpson's rule was applied on m subintervals of $c(x) \le y \le d(x)$ to $f(x,y)$ and this

internal integral expression was defined as the function $F(x)$. Then, Simpson's rule was reapplied on n subintervals of $a \le x \le b$ to $F(x)$. To calculate the far-field components of the electric field of Equation 4-3 and Equation 4-4, a function named *get_far_field(.....)* was implemented in C++. The *get_far_field(.....)* creates a data file *far_field.dat*, which contains the θ and ϕ components of the far-field.

5 Results

5.1 Introduction

The main purpose of this thesis is to investigate the performance parameters of the anisotropic PML and the use of PML in horn antenna analysis, using high-order hierarchal edge element. All the examples chosen are either easy to solve analytically or their measured values are known. Thus, the program outputs can be compared with the measured or analytical values for validation purpose.

The results shown in this thesis have been obtained by using the hierarchal tetrahedral edge elements described by Webb [19]. The order of the element is designated by a pair of indices, (g,r), where g is the order of the gradient space (G_g) and r is the order of the rotational space (R_r). Since the convergence rate is limited by the order of the curl, reducing the gradient space by one order should leave the convergence rate unchanged. This is also called the reduced-gradient spaces: $(g,r) = (0,1), (1,2), (2,3), ...(p-1,p)$. The $(p-1,p)$ element has the same asymptotic convergence rate as the (p,p) element [19].

Also note that all graphs shown in this chapter have been obtained by using Microsoft Excel's "Standard Types – XY (Scatter)" [26] chart type.

5.2 Parallel Plate TEM waveguide

A y-polarized TEM wave propagating in the $+z$-direction along a uniform parallel-plate transmission line as shown in Figure 5-1 has been considered. For time-harmonic fields, the wave equation to be satisfied in the sourceless dielectric region becomes the homogeneous Helmholtz's equation [24]

Equation 5-1 $$\nabla^2 \overline{E} - \gamma^2 \overline{E} = 0$$

where $\overline{E}$ is the electric field and γ is the propagation constant of the wave. In the present

case, the appropriate phasor solution for the wave propagating in the $+z$ direction is

Equation 5-2
$$\overline{E} = \hat{a}_y E_y = \hat{a}_y E_0 e^{-\gamma z}$$

The associated magnetic field $\overline{H}$ is of the form

Equation 5-3
$$\overline{H} = \hat{a}_x H_x = -\hat{a}_x \frac{E_0}{\eta} e^{-\gamma z}$$

where η is the intrinsic impedance of the dielectric medium, defined as

Equation 5-4
$$\eta = \sqrt{\frac{\mu}{\varepsilon}}$$

where μ and ε are the permeability and the permittivity, respectively, of the dielectric medium.

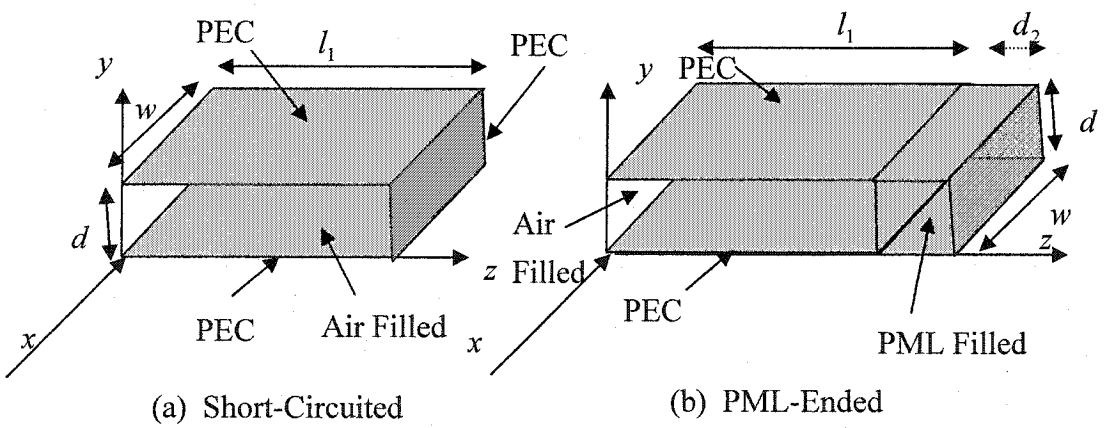

Figure 5-1: Short-Circuited and PML-Ended parallel plate

For parallel plate transmission lines the inductance L, capacitance C, conductance G, and the resistance R per unit length can be given as [24]

Equation 5-5
$$L = \frac{\mu d}{w}$$

Equation 5-6 $$C = \frac{\varepsilon' w}{d}$$

Equation 5-7 $$R = \frac{2R_s}{w}$$

Equation 5-8 $$G = \frac{\varpi \varepsilon'' w}{d}$$

where d and w are the length and width, respectively, of the parallel plate as shown in Figure 5-1; $\varepsilon = \varepsilon' - j\varepsilon''$ is the permittivity, and R_S is the surface resistivity of the plate. Propagation constant γ is defined as [24]

Equation 5-9 $$\gamma = \alpha + j\beta = \sqrt{(R + j\varpi L)(G + j\varpi C)}$$

where α is the attenuation constant and β is the phase constant. For the lossless case, $R = G = 0$. Using Equation 5-5, Equation 5-6, Equation 5-7, and Equation 5-8, Equation 5-9 can be rewritten as

Equation 5-10 $$\gamma = \alpha + j\beta = j\varpi\sqrt{LC} = j\varpi\sqrt{\mu\varepsilon'} = j\varpi\sqrt{\mu\varepsilon}$$

The characteristic impedance Z_{th} of the lossless parallel plate shown in Figure 5-1 is given as [24]

Equation 5-11 $$Z_{th} = \frac{d}{w}\sqrt{\frac{\mu}{\varepsilon}} = \frac{d}{w}\eta$$

In terms of characteristic impedance of a two wire transmission line, Figure 5-1 can be redrawn as

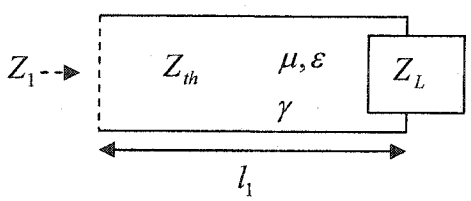

Figure 5-2: Parallel plate in terms of impedance

where Z_L is the load impedance (for PEC $Z_L = 0$, for PMC $Z_L = \infty$, and for PML

$Z_L = Z_{th}$), l_1 is the length of the waveguide in z -direction, Z_1 is the equivalent impedance at the input port. At the source end of the line, the source looking towards the load sees the input impedance Z_1 [24] given by

Equation 5-12

$$Z_1 = Z_{th} \frac{Z_L + Z_{th} \tanh \gamma l_1}{Z_{th} + Z_L \tanh \gamma l_1}$$

Using Equation 5-10, Equation 5-12 can be simplified to

Equation 5-13

$$Z_1 = Z_{th} \frac{Z_L + jZ_{th} \tan \beta l_1}{Z_{th} + jZ_L \tan \beta l_1}$$

The reflection coefficient Γ_{in} or S_{11} at the input end of the waveguide is [24]

Equation 5-14

$$\Gamma_{in} = S_{11} = \frac{Z_1 - Z_{th}}{Z_1 + Z_{th}}$$

If the parallel plate is terminated with PEC or PMC, the characteristic impedance Z_L of the load is zero or infinity, respectively. From Equation 5-14, the magnitude of the reflection coefficient Γ_{in} for short-circuited (PEC) or open-circuited (PMC) parallel plate becomes 1.

The material property of PML is assigned in such a way so that the characteristic impedance Z_{th} is the same as the load impedance Z_L (in this case the PML) as mentioned in chapter 3. So, from Equation 5-14, the reflection coefficient Γ_{in} for PML ended parallel plate becomes zero as it should, as explained in chapter 3.

5.2.1 Short-Circuited S_{11}

The reflection coefficient at the input end of the parallel plate waveguide shown in Figure 5-1 (a) with $d = 2\,\text{m}, w = 1\,\text{m}$, and $l_1 = 10\,\text{m}$ at frequency $f = 60\,\text{MHz}$ has been studied. At the opposite end, PEC has been used. This is a preliminary experiment to ensure that the setup of the problem is done properly and the FEM gives the right solutions for the real and imaginary part of the reflection coefficient.

First, the effect of the element size, by adjusting the length of the longest edge, is demonstrated, by keeping all other parameters the same. Note that the $(1,2)$ order basis function has been used for each element. From Figure 5-3 , it can be observed that as the element size gets smaller, the experimental results become closer to the analytical results, as expected.

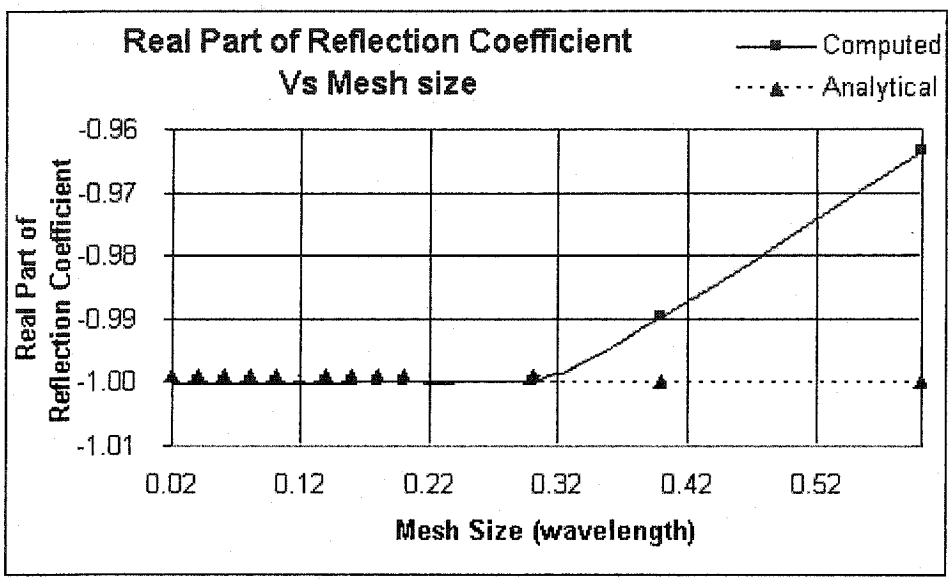

(a)

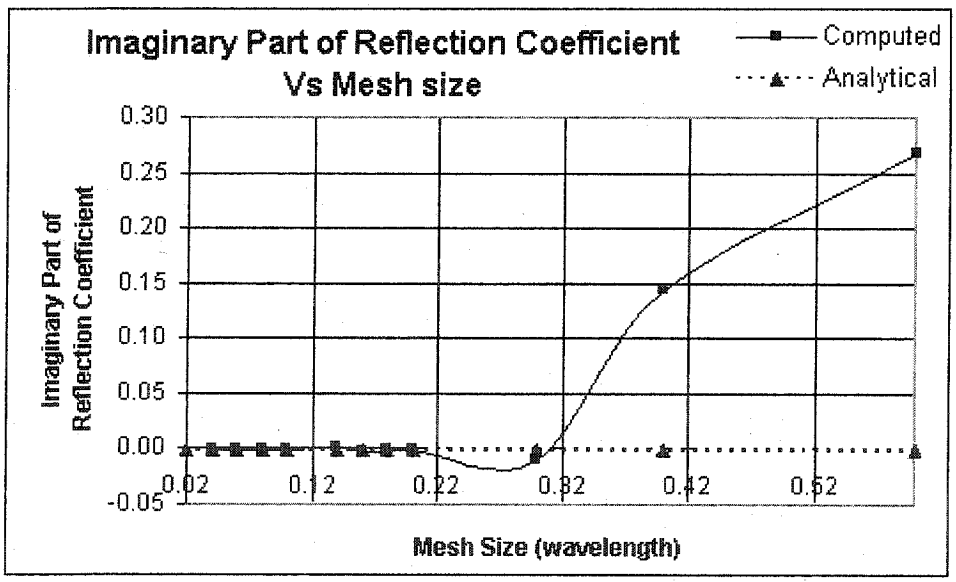

(b)

Figure 5-3: Reflection Coefficient Vs Element Size. (a) Real Part, and (b) Imaginary Part

The effect of the order of the basis function is illustrated in Figure 5-4. Note that element size of 0.1λ has been used as it provided good results as shown in the previous experiment.

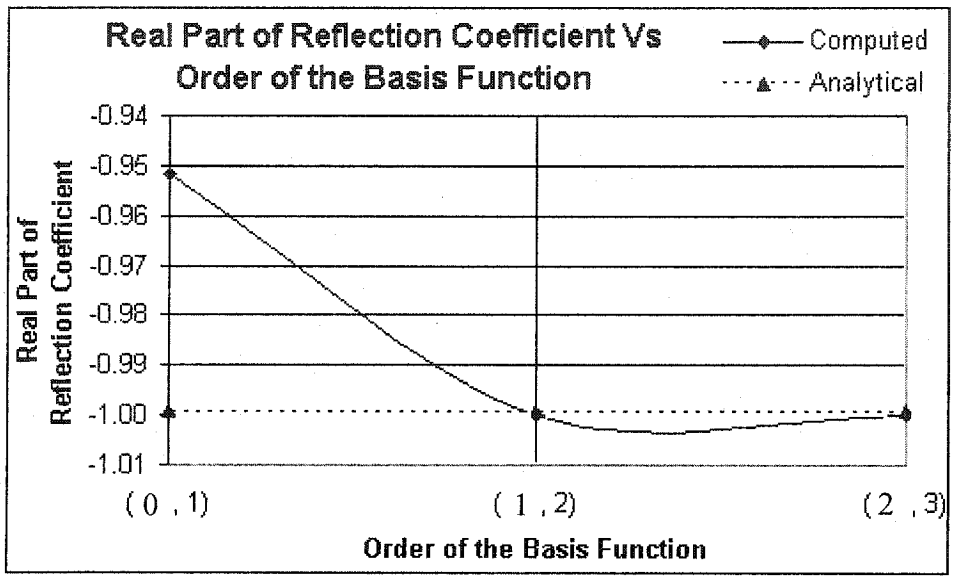

(a)

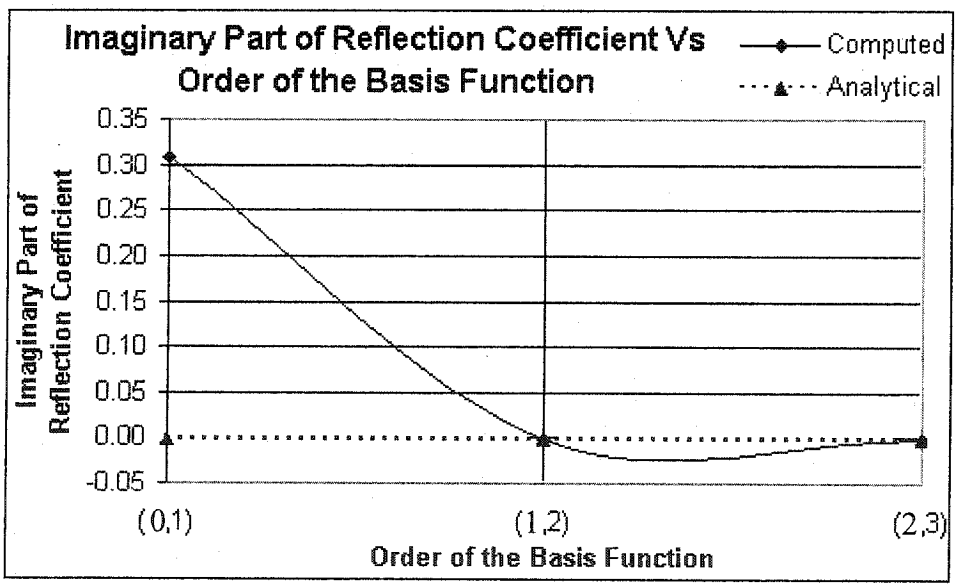

(b)

Figure 5-4: Reflection Coefficient Vs Order of the Basis Function.

(a) Real Part, and (b) Imaginary Part.

From the figure it can be seen that as the order of the basis function increases, the

solution accuracy also increases. It is known that as the order of the basis function increases, the number of unknowns increase, which in turn increases the computational cost, defined as the number of unknowns multiplied with the number of iterations. So, there has to be a compromise between computational cost and solution accuracy. In fact, solution accuracy can be increased by either reducing the mesh size (*h*-adaption) or by increasing the order of the basis function (*p*-adaption) or both (*h-p* adaption). The FEM solution of this problem is compared to the analytic solution and a good agreement is observed, which demonstrates that the setup of the problem and the hierarchal edge based FEM are working properly.

5.2.2 PML-Ended S_{11}

In this example, the same waveguide of section 5.2.1 is used, but with a metal backed PML layer instead of PEC at the opposite end, as shown in Figure 5-1 (b). The effects of changing the values of the width d_2 of the PML layer and the material properties s' and s'' as defined in chapter 3 are explored. In these experiments, $d_2 = 5\,\text{m}$, the element size is 0.2 m and $(2,3)$ order basis functions have been used. This is just a preliminary experiment to observe if the PML is doing what it is supposed to do. As the purpose of the PML is to absorb the incident wave, the return loss, which is $20\log_{10} | S_{11} |$, should be as small as possible.

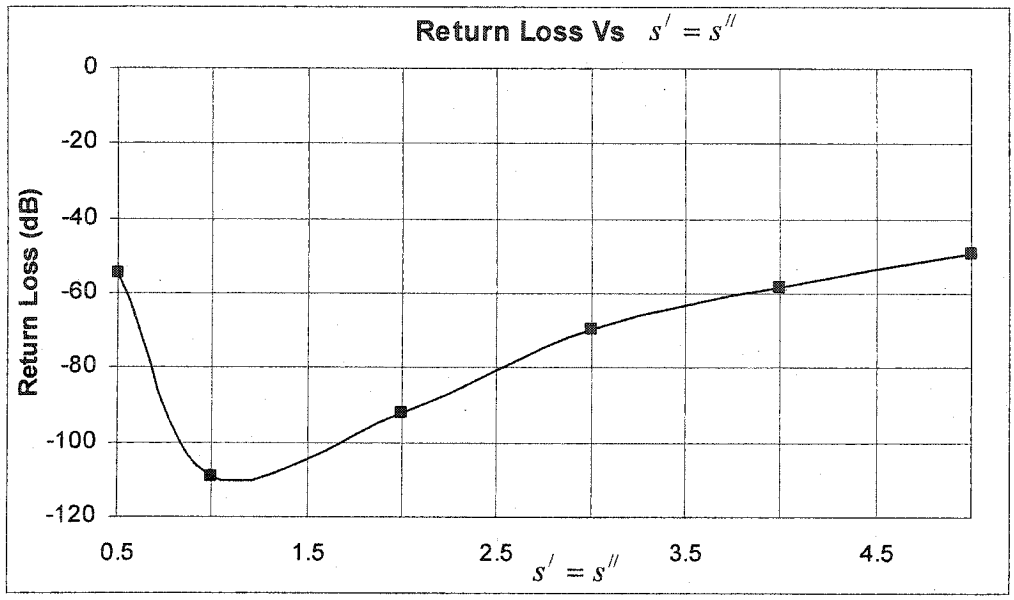

Figure 5-5: Return Loss Vs $s' = s''$

The effect of the material properties s' and s'' can be observed in Figure 5-5. The value $s' = s''$ has been used to improve the convergence rate as explained in chapter 3. The return loss shown in Figure 5-5 is a very small number as expected. From Figure 5-5, it can be seen that the patterns keep changing as the values of s' and s'' are increased. However, after a particular value of s' and s'', any larger values of s' and s'' do not improve the solution accuracy very much. In fact, larger values of s' and s'' result in larger discretization errors due to the fact that the fields inside the PML region change more and more drastically and the mesh becomes less and less capable of modeling them correctly. It has been observed that for a fine mesh there exists a range of values for s' and s'' that results in good absorption.

5.3 Rectangular Wave-Guide

In this case the wave propagating along a straight guiding structure with a uniform rectangular cross section of sides a and b as shown in Figure 5-6 has been considered.

Suppose the waves propagate in the $+z$-direction with propagation constant γ. In general, γ is a complex number:

Equation 5-15 $$\gamma = \alpha + j\beta$$

For lossless transmission line γ becomes purely imaginary:

Equation 5-16 $$\gamma = j\beta$$

For TE wave, the transverse component of the electric field E_Z is zero. The transverse component of magnetic field $H_Z = H_z^0(x,y)e^{-\gamma z}$ can be solved by using the following Helmholtz's equation [24].

Equation 5-17 $$\nabla_{xy}^2 H_z^0 + (\gamma^2 + k^2)H_z^0 = 0$$

where k is the wavenumber defined as:

Equation 5-18 $$k = \varpi\sqrt{\mu\varepsilon}$$

where frequency $\varpi = 2\pi f$, $f = \frac{u}{\lambda}$ and velocity $u = \frac{1}{\sqrt{\mu\varepsilon}}$

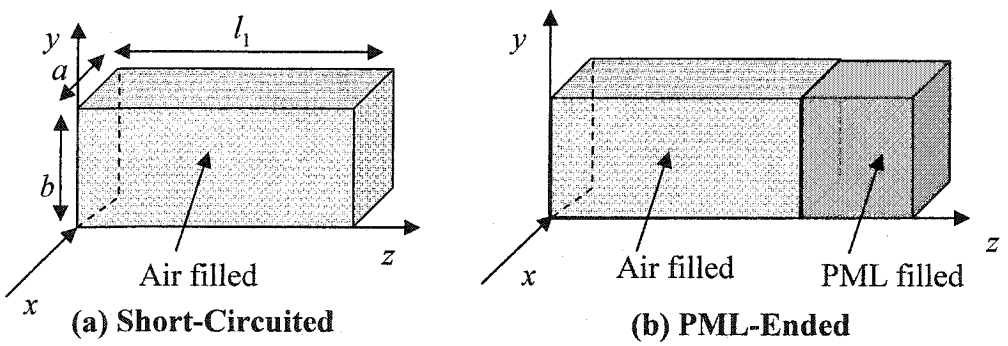

Figure 5-6: Short-Circuited and PML-Ended Rectangular Waveguide

For TE_{mn}, γ can be solved as [24]

Equation 5-19 $$\gamma = j\beta = j\sqrt{\varpi^2\mu\varepsilon - \left(\frac{m\pi}{a}\right)^2 - \left(\frac{n\pi}{b}\right)^2}$$

Every combination of the integers m and n defines a possible mode that may be designated as the TE_{mn} mode; thus there are a doubly infinite number of TE modes. Using

Equation 5-18, Equation 5-19 can be rewritten as

Equation 5-20

$$\gamma = j\beta = j\sqrt{4\pi^2 f^2 \mu\varepsilon - \left(\frac{m\pi}{a}\right)^2 - \left(\frac{n\pi}{b}\right)^2}$$

The frequency f_c, at which $\gamma = 0$ is called the cutoff frequency. So, from Equation 5-20, f_c can be derived as

Equation 5-21

$$(f_c)_{mn} = \frac{1}{2\sqrt{\mu\varepsilon}}\sqrt{\left(\frac{m}{a}\right)^2 + \left(\frac{n}{b}\right)^2}$$

Waves of frequencies below the cutoff frequency of a particular mode cannot propagate, and the power and signal transmission at the mode is possible only for frequencies higher than the cutoff frequency. If $a > b$, the cutoff frequency f_c is the lowest when $m = 1$ and $n = 0$:

Equation 5-22

$$(f_c)_{10} = \frac{1}{2\sqrt{\mu\varepsilon}}\sqrt{\left(\frac{1}{a}\right)^2} = \frac{u}{2a}$$

Hence the TE_{10} mode is the dominant mode of a rectangular waveguide with $a > b$. Because the TE_{10} mode has the lowest attenuation of all modes in a rectangular waveguide and its electric field is in one direction everywhere, it is of particular practical importance [24].

The wave impedance Z_{th} for the TE waves can be written as [24]

Equation 5-23

$$Z_{th} = \frac{\eta}{\sqrt{1 - \left(\frac{f_c}{f}\right)^2}}$$

Using Equation 5-4 and Equation 5-22, Equation 5-23 can be rewritten as

Equation 5-24

$$Z_{th} = \sqrt{\frac{\mu}{\varepsilon}}\left[1 - \left(\frac{\lambda}{2a}\right)^2\right]^{-\frac{1}{2}}$$

In terms of the characteristic impedance of the two wire transmission line, Figure 5-6 can

be redrawn as Figure 5-2. So, the equation for calculating the reflection coefficient will be the same as Equation 5-14, where Z_1 is obtained from Equation 5-12 or Equation 5-13, and Z_{th} is obtained from Equation 5-24.

5.3.1 Short-Circuited S_{11}

The reflection coefficient at the input end of a rectangular waveguide shown in Figure 5-6 with $a = 0.0157988\,\text{m}$, $b = 0.0078994\,\text{m}$, and length $l_1 = 0.02286\,\text{m}$ at frequency 13.997GHz has been studied. At the opposite end, PEC has been used. This is a preliminary experiment using rectangular waveguide to ensure that the setup has been done properly and the FEM gives the right solutions for the real and imaginary parts of the reflection coefficient, as it will be used in the following examples as the feed. The effect of the element size and the order of the basis function on the solution accuracy are illustrated here.

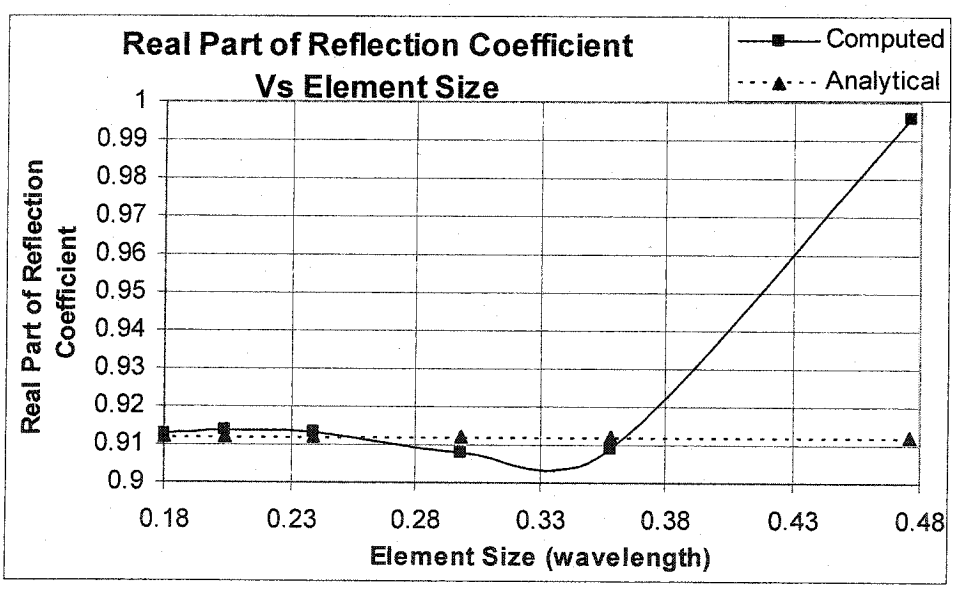

(a)

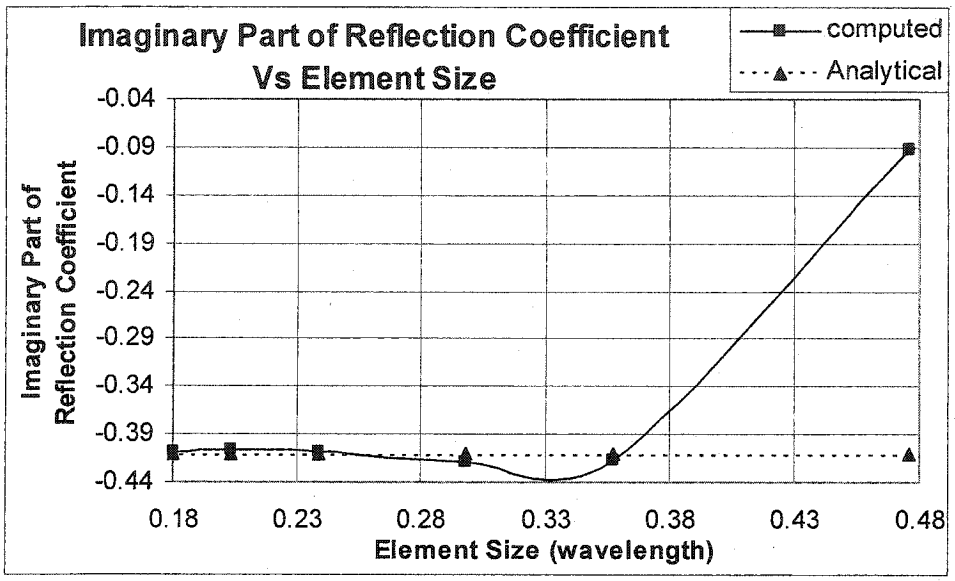

(b)

Figure 5-7: Reflection Coefficient Vs Element Size. (a) Real Part (b) Imaginary Part. Used (2, 3) Order Basis Function.

First, the effect of element size on the FEM solution is illustrated. In particular, six different sizes of elements (0.18, 0.20, 0.24, 0.30, 0.36, and 0.48 wavelength) have been selected for illustration. Note that $(2,3)$ order basis functions have been used for all six sizes of the elements. From Figure 5-7 it is seen that as the element size becomes smaller, the computed results become closer to the analytical results. A smaller sized element keeps the discretization error small. However, as the element size becomes smaller, degrees of freedom increases. So, computational cost becomes more significant.

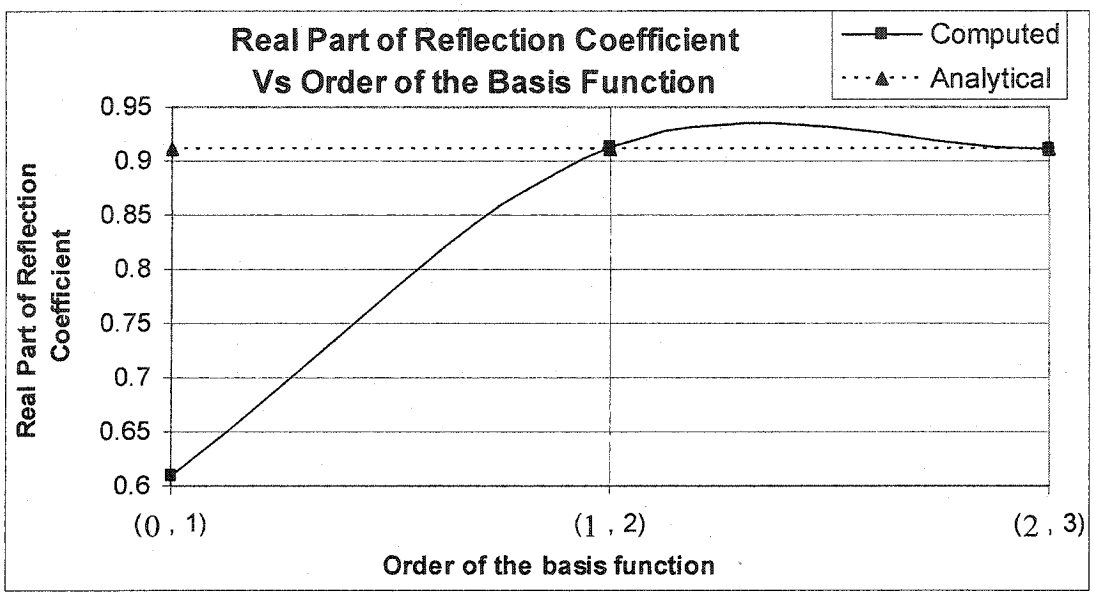

(a)

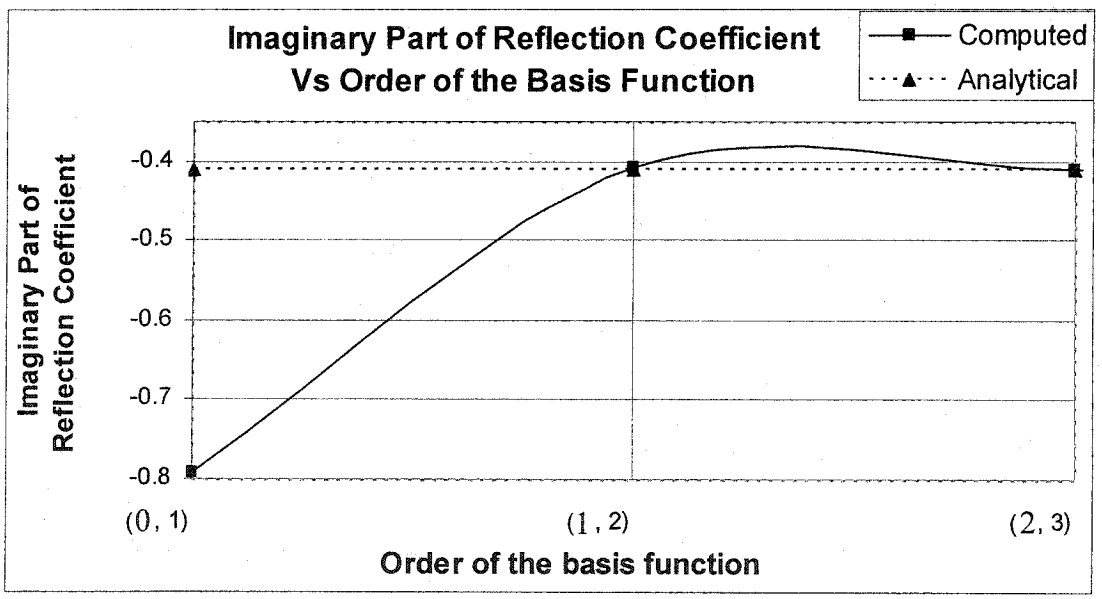

(b)

Figure 5-8: Reflection Coefficient Vs Order of the Basis Function. (a) Real Part (b) Imaginary Part. Used Element Size of 0.24λ

In this case, element size of 0.30λ gives comparatively accurate results for a relatively low computational cost. Further decreasing the element size does not improve the solution accuracy as much compared to the computational cost. The best element size depends on the problem geometry, the order of the basis function, and the accuracy one is

looking for.

Next the effect of the order of the basis function has been tested. In particular, four different orders ((0, 1), (1, 2), and (2, 3)) have been selected for illustration. Note that element size of 0.24λ has been used for all four orders. It can be seen from Figure 5-8 that the solution accuracy increases as the order of the basis function increases. However, as the order of the basis function becomes higher, computational cost becomes more significant. So, there has to be a compromise between solution accuracy and computational cost. In this case, the (2,3) order basis function gives an almost accurate solution. Further increasing the order of the basis function does not have any significant effect on the solution accuracy as the computed and analytical results are already overlapping. In practice, the choice of the order of the basis function must be made in conjunction with the element size. For a sufficiently fine mesh, a lower order basis function can be used. For a relatively coarse mesh, higher order basis functions must be used to get accurate results. But if the mesh is too coarse, increasing the order of the basis function will not provide accurate results.

These results suggest that there is a compromise between solution accuracy and computational cost. Smaller element size gives higher accuracy but requires more computational resources. Higher order polynomials give higher accuracy and require more computational resource. In this case, it can be seen that element size of 0.24λ with (2,3) order basis gives very accurate results with comparatively low computational cost.

5.3.2 PML-Ended S_{11}

In this case, the waveguide of the same dimensions as of Section 5.3.1 has been used. But, at the opposite end, instead of PEC, a metal backed PML layer has been used as shown in Figure 5-6. In the next couple of experiments, PML surrounded scattering problems will be considered, by using various values of the width d_2 of the PML layer and material properties s' and s'', in order to find values that will provide very good absorption for comparatively lower computational cost.

In this part, the effect of the width d_2 of the PML layer is observed with the same material property $s' = s'' = 1$, element size 0.24λ and the order of the basis function (2, 3).

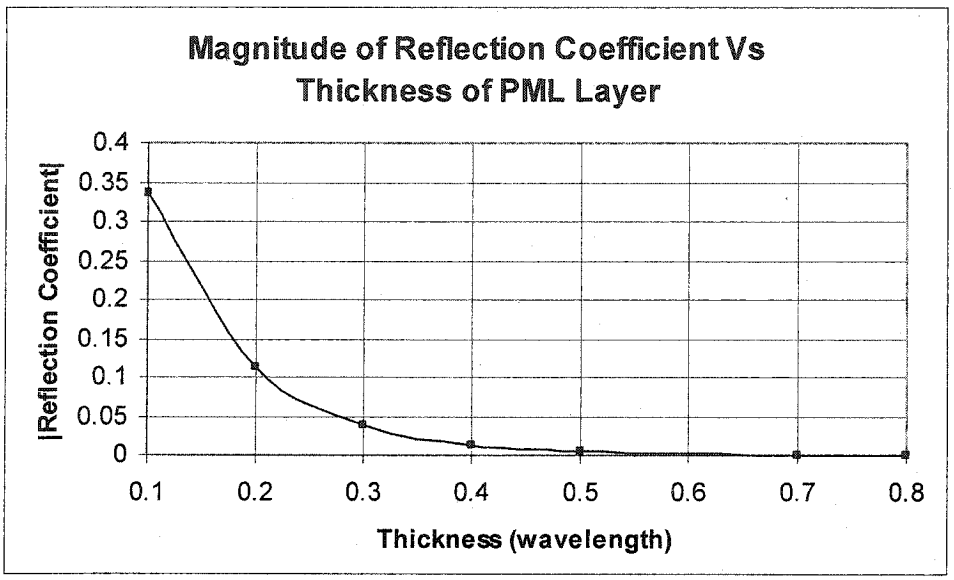

Figure 5-9: Reflection Coefficient Vs Thickness d_2 of the PML Layer

In this case, eight different values for d_2 (0.12, 0.24, 0.36, 0.47, 0.59, 0.83, and 0.95 wavelength) have been selected for illustration. Figure 5-9 shows that as the thickness d_2 of the PML layer is increased, the absorbing capability of the PML is increased. In this case, thickness of 0.59λ gives almost perfect absorption. Further increasing the thickness does not improve the absorbing capability significantly as the reflection coefficient is almost already the lowest. From Figure 5-10 it can be observed that as the

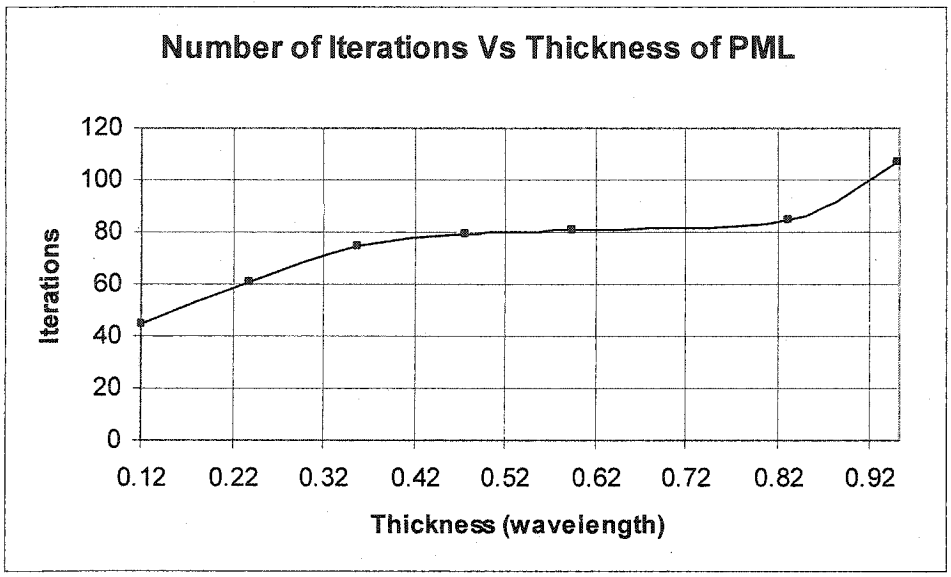

Figure 5-10: Iteration Vs the thickness of the PML Layer.

thickness d_2 of the PML layer is increased, the number of iterations are increased. So, there has to be a compromise between computational cost and absorption capability. But, by carefully choosing the thickness d_2, it is possible to obtain a very good absorption for lower computational cost. In this case, it can be concluded that the thickness $d_2 = 0.59\lambda$ provides very good absorption for a comparatively low computational cost.

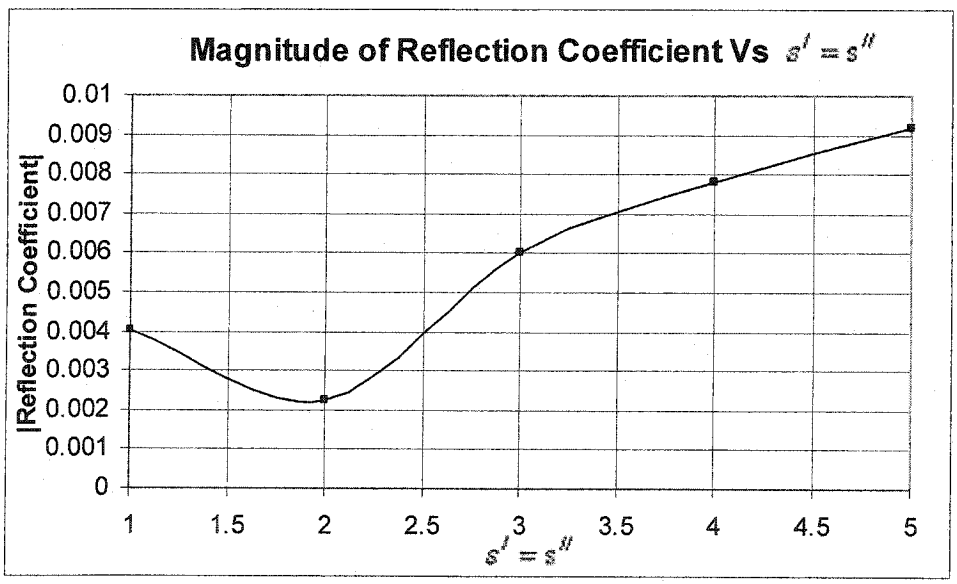

Figure 5-11: Reflection Coefficient Vs $s^{/} = s^{//}$

The effects of the PML material properties s' and s'' on the absorption capability and the resulting computational cost have been tested. To find out how s' and s'' affect the performance of the PML, all parameters have been kept the same as before, and the thickness of the PML layer $d_2 = 0.59\lambda$ has been used. Figure 5-11 shows that $s' = s'' = 1.85$ gives the best absorption. It is observed that there is a range of values for s' and s'' for which the reflection coefficient is very small. Larger values of s' and s'' result in larger number of iterations as shown in Figure 5-12. In fact, larger values of s' and s'' result in larger discretization errors due to the fact that the fields inside the PML region change more and more drastically and the mesh becomes less and less capable to model them correctly. In this case, $s' = s'' = 1$ provides very good absorption for comparatively low computational cost.

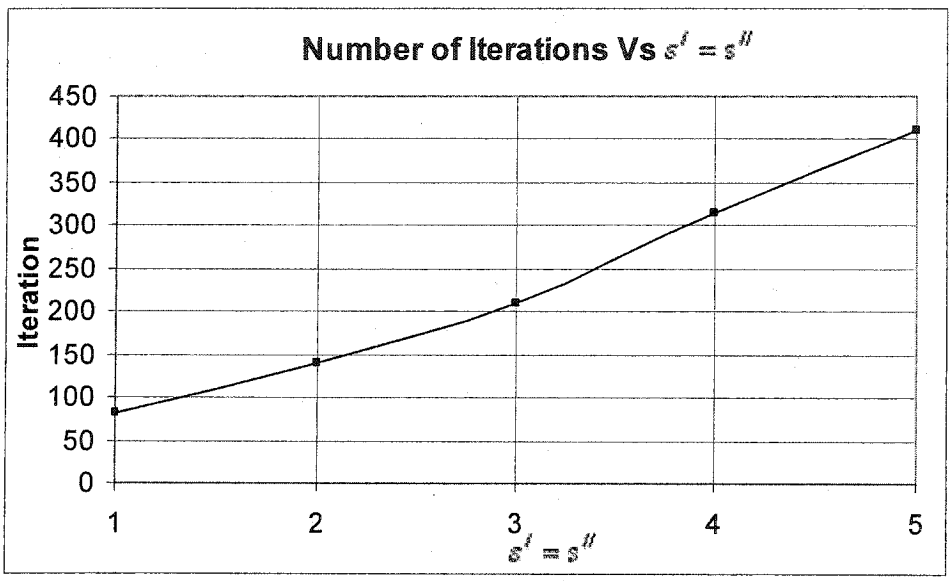

Figure 5-12: Number of Iterations Vs $s' = s''$

5.4 Waveguide with Flange in Rectangular PML Box

A flange terminated rectangular waveguide surrounded by a PML box as shown in Figure 5-13 has been considered. In this example, from the experimental value of S_{11}, the

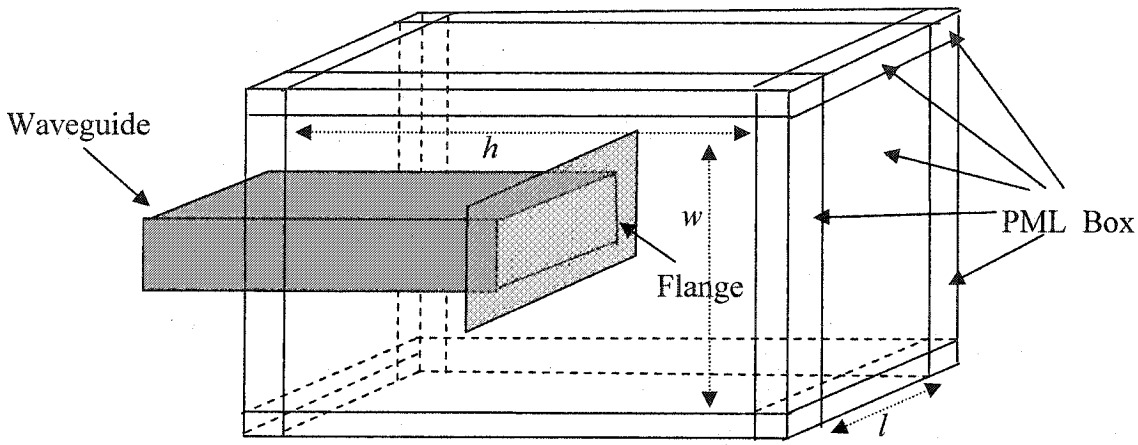

Figure 5-13: Flange inside Rectangular PML Box

aperture impedance has been calculated and then compared with the measured values. Equation 5-14 can be rewritten as

Equation 5-25

$$S_{11} = \Gamma_{in} = \frac{Z_c - 1}{Z_c + 1}$$

where $Z_c = \frac{Z_1}{Z_{th}}$ is the normalized impedance. From Equation 5-25 the value of Z_c can be derived as

Equation 5-26

$$Z_c = \frac{1 + S_{11}}{1 - S_{11}}$$

5.4.1 Verifying S_{11}

In this example, the reflection coefficient at the input end of a rectangular waveguide of dimensions $a = 1.57988$ cm, $b = 0.78994$ cm, and with a flange at the end of dimension 3.3655×3.3655 cm^2 as shown in Figure 5-13 has been studied. The rectangular waveguide with the flange has been surrounded by a rectangular PML box of inner dimensions of length $l = 4.3815$ cm (parallel to $x-axis$), width $w = 4.3815$ cm (parallel to $y-axis$), height $h = 2.54$ cm (parallel to $z-axis$), as shown in Figure 5-13, and the distance between the flange (aperture) and the inner side of the PML box is $d_1 = 1.016$ cm, with the cross-sectional view given as in Figure 3-3. The material property of the PML box has $s^{/} = s^{//} = 1$.

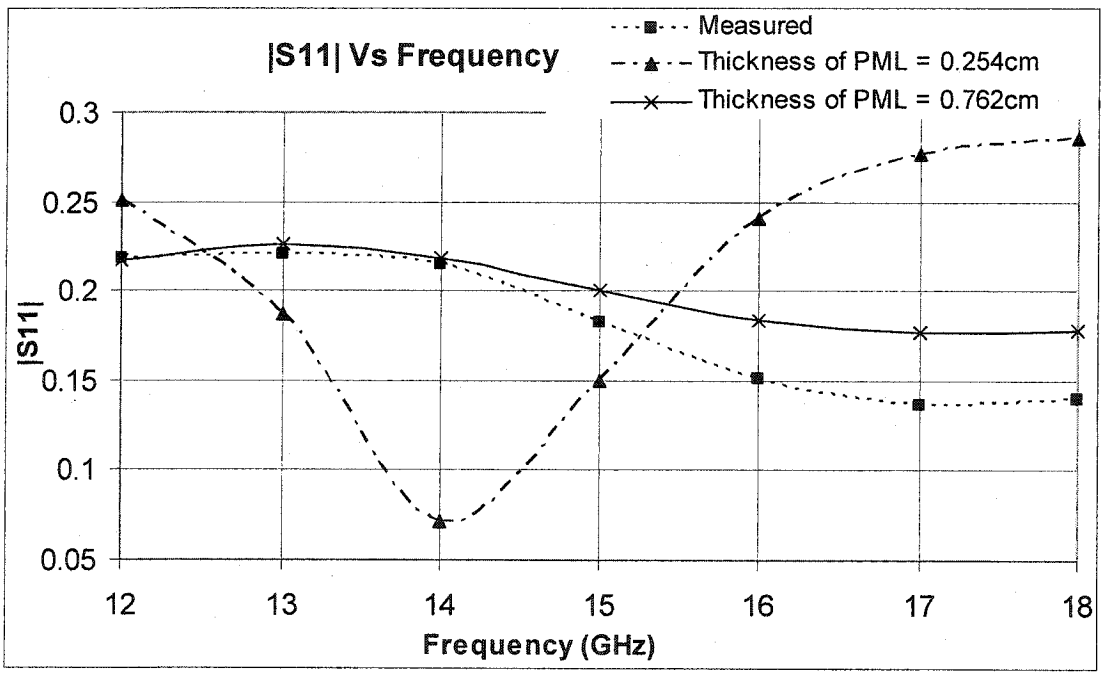

Figure 5-14: Amplitude of Reflection Coefficient Vs Frequency.

First, the effect of the thickness d_2 of the PML box as shown in the cross-sectional view of Figure 3-3 is illustrated. In particular, two different values of d_2 (0.254 and 0.762 cm) have been selected for illustration. Note that the element size of 0.2 cm and (2,3) order basis functions have been used in all the cases. Figure 5-14 shows the comparison between the computed and measured reflections for the TE_{10} incident mode. From Figure 5-14, it is clear that as the thickness of the PML increases, computed results become closer to the measured results, as expected. The computed results of thickness

$d_2 = 0.762$ cm are in good agreement with the measured values.

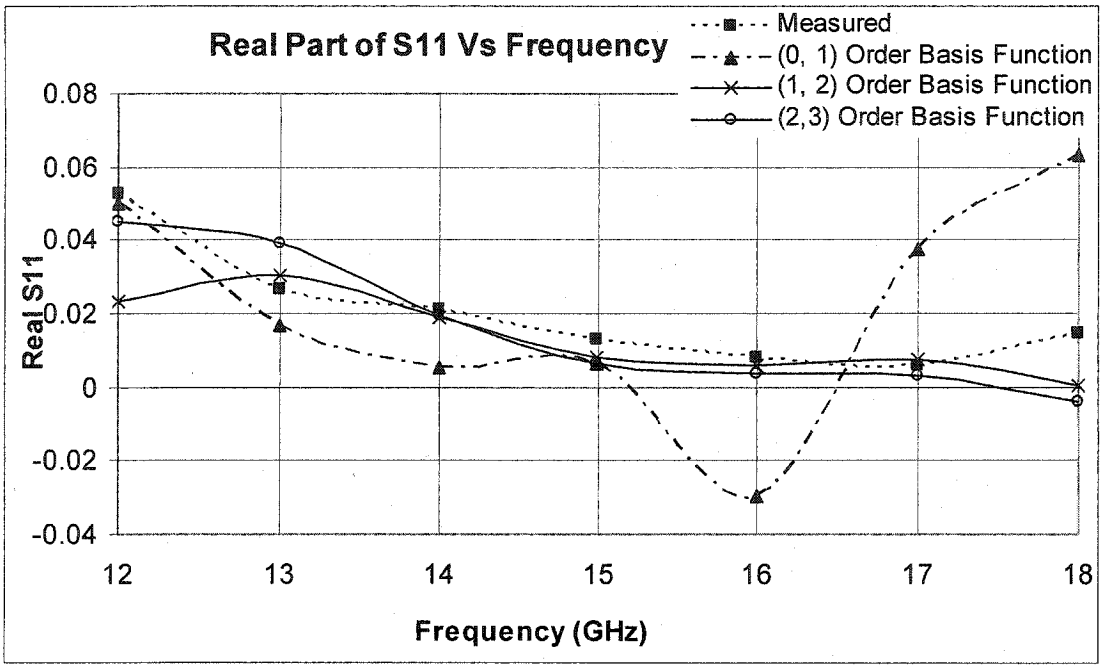

(a)

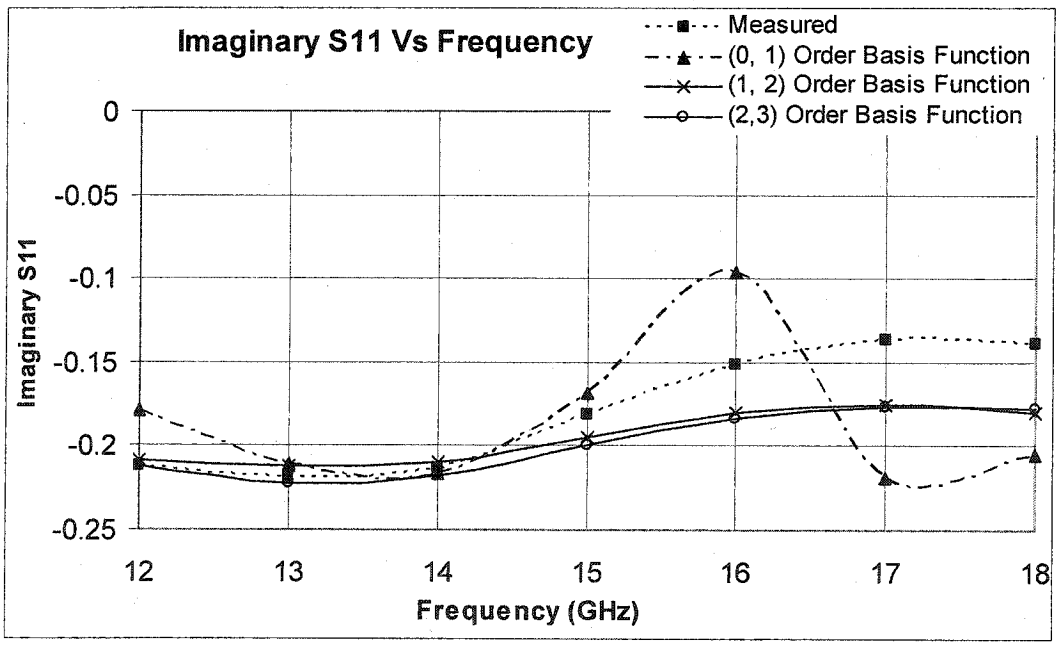

(b)

Figure 5-15: Reflection Coefficient Vs Frequency. (a) Real Part (b) Imaginary Part.

The effect of the order of the basis function has also been tested. The PML box has the same dimensions as the previous experiment along with the thickness of the PML box $d_2 = 0.254$ cm. In particular, three different orders ((0, 1), (1, 2), and (2, 3)) have been selected for illustration. Note that element size of 0.2 cm has been used in all cases. Figure 5-15 (a) and (b) show the comparison between the computed and the measured real and imaginary parts of the reflection for the TE_{10} incident mode. From the figure, it is clear that as the order of the basis function increases, computed results become closer to the measured results. From the figure, it can also be observed that as the frequency increases, discrepancy between the measured and the computed result increases due to the fact that higher frequency requires a smaller element.

5.4.2 Normalized aperture impedance

Using Equation 5-26, normalized impedance has been derived and compared with the measured value [4]. Results of section 5.4.1 have been used to derive the impedances from reflection coefficients. The FEM provides an excellent solution, which is almost indistinguishable from the measured value. These results validate the behavior of the PML.

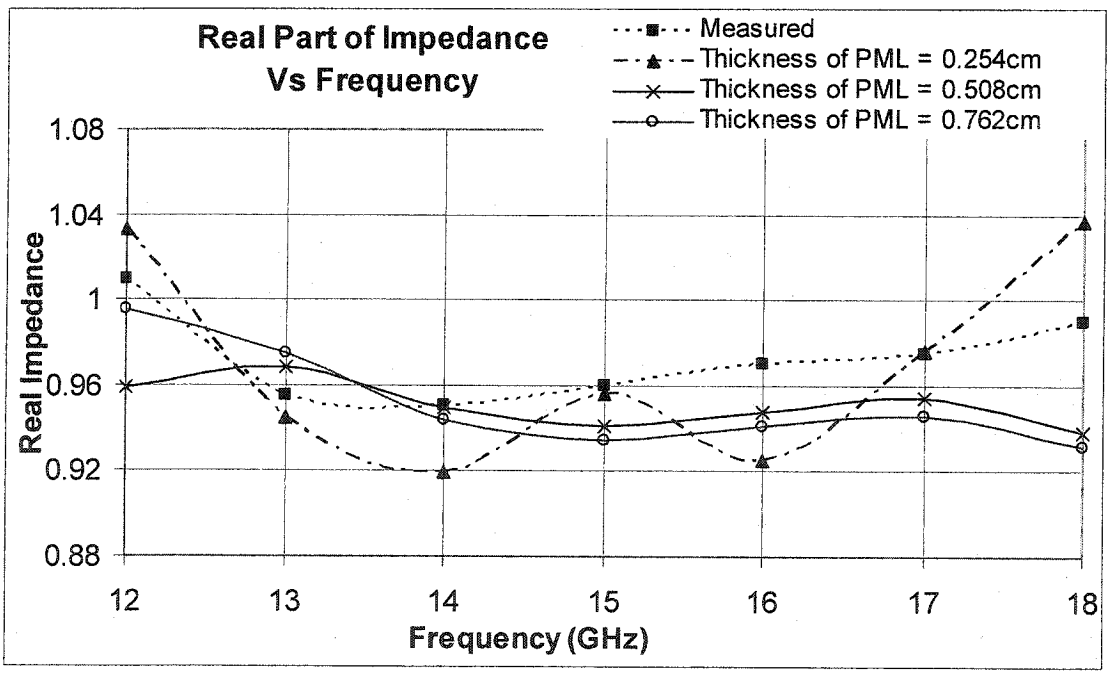

(a)

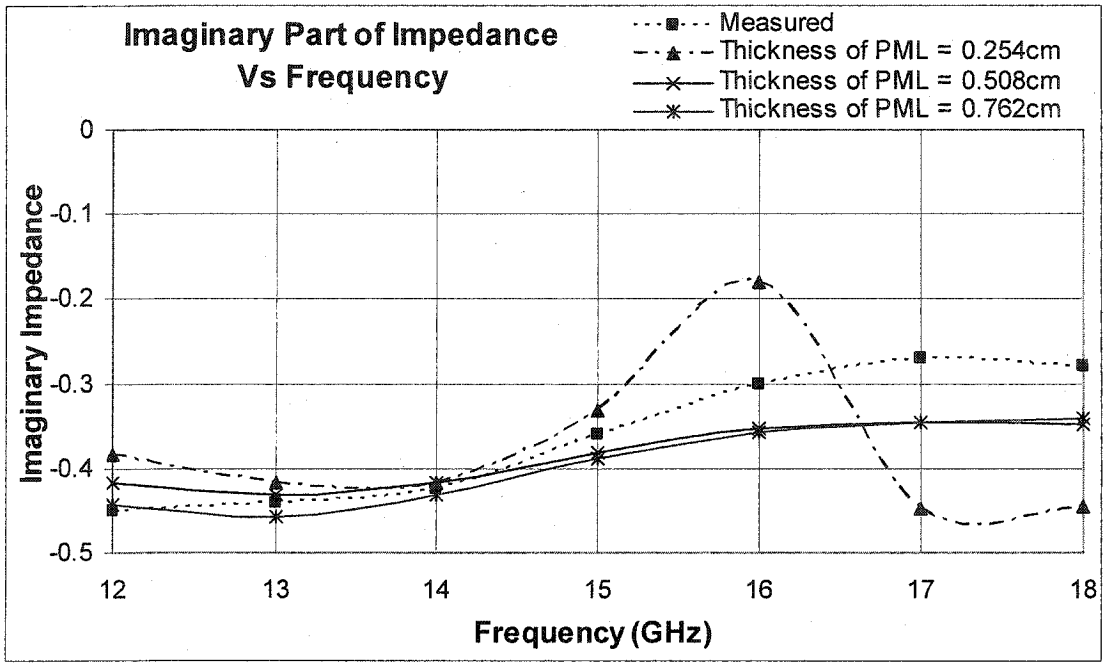

(b)

Figure 5-16: Impedance Vs Frequency. (a) Real Part (b) Imaginary Part.

Figure 5-16 shows the comparison between computed and measured real and imaginary parts of the aperture impedance for the TE_{10} incident mode. There is good agreement between the measured and the computed results.

5.5 Waveguide with Horn in Rectangular PML Box

A horn terminated rectangular waveguide surrounded by a PML box as shown in Equation 5-17 has been considered. As the horn is inside the PML box, there should not be any reflection from the interface of the PML box and air.

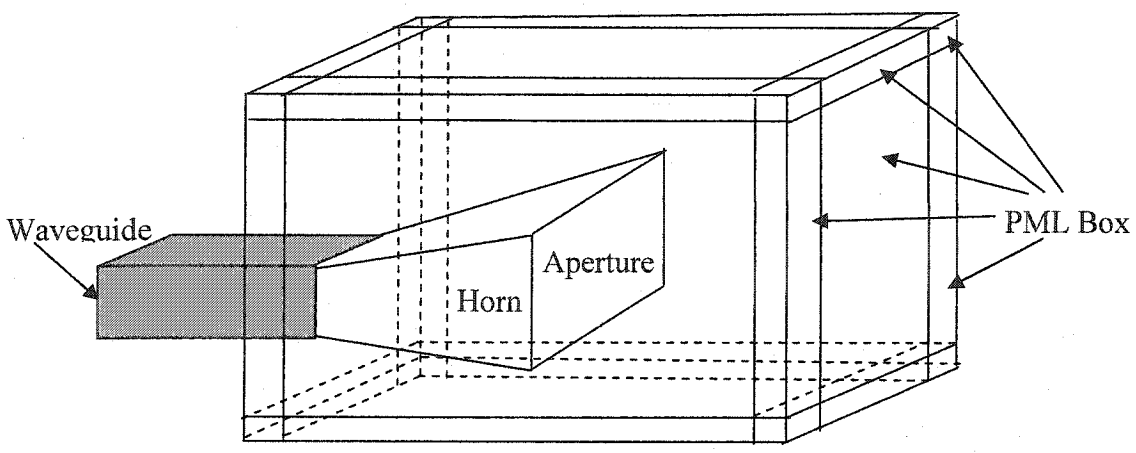

Figure 5-17: Horn inside Rectangular PML Box

There will be reflection because of the impedance mismatch at the interface of the aperture of the horn and the air. As the horn has larger flare dimensions than the flange, it will have less reflection. To make sure everything has been set-up properly, the input return loss has been compared with the measured values. Finally, the experimental value of the far field radiation pattern has been compared with the measured value.

5.5.1 Input Return Loss

In this experiment, a pyramidal horn of wave guide dimension 0.01905×0.009525 m^2, aperture dimension 0.034417×0.034417 m^2, and length 0.077724 m has been analyzed. The rectangular waveguide with the flange has been surrounded by a rectangular PML box of inner dimensions of length $l = 0.043815$ m (parallel to $x-axis$), width $w = 0.043815$ m (parallel to $y-axis$) , height $h = 0.1143$ m (parallel to $z-axis$) as shown in Figure 5-13, distance $d_1 = 0.01016$ m between the horn aperture and the inner side of the PML box as shown in the cross-sectional view of Figure 3-3. The material properties s' and s'' of the PML box have been assigned to be $s' = s'' = 1$. From the experimental value of the reflection coefficient, the return loss has been calculated and compared with the measured value [4].

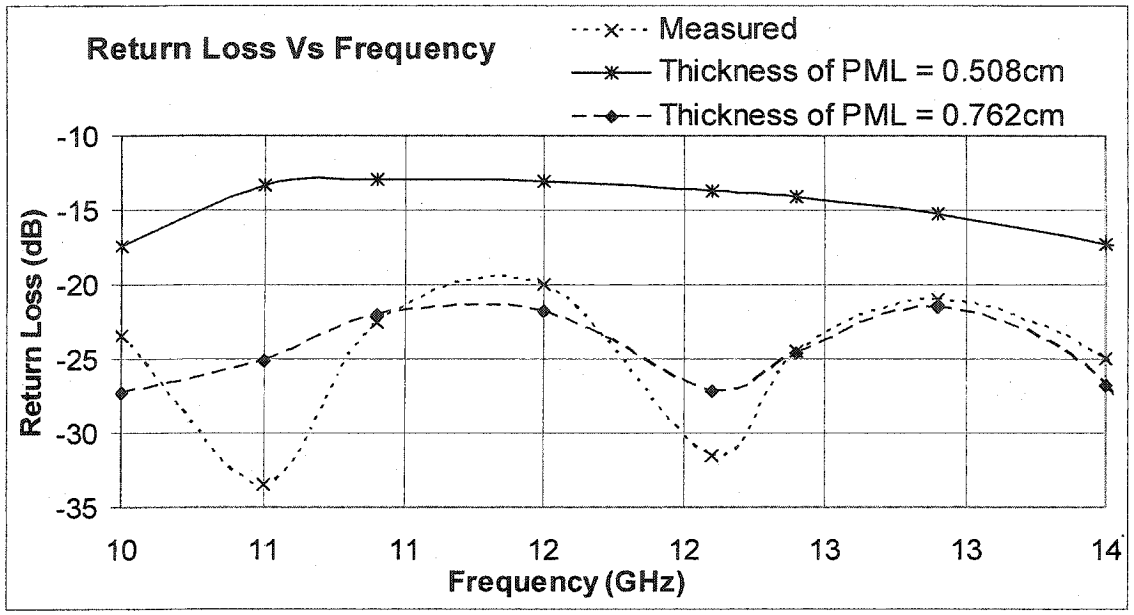

Figure 5-18: Return Loss Vs Frequency.

Figure 5-18 shows the comparison between computed and measured Return Loss values for the TE_{10} incident mode. Note that (1, 2) order basis function has been used. From the figure, it is clear that as the thickness of the PML increases, computed results become closer to the measured results. From Figure 5-18 it can be observed that as the frequency gets higher, measured values become closer to the computed values due to the fact that higher frequency requires thinner PML layer for the same absorption.

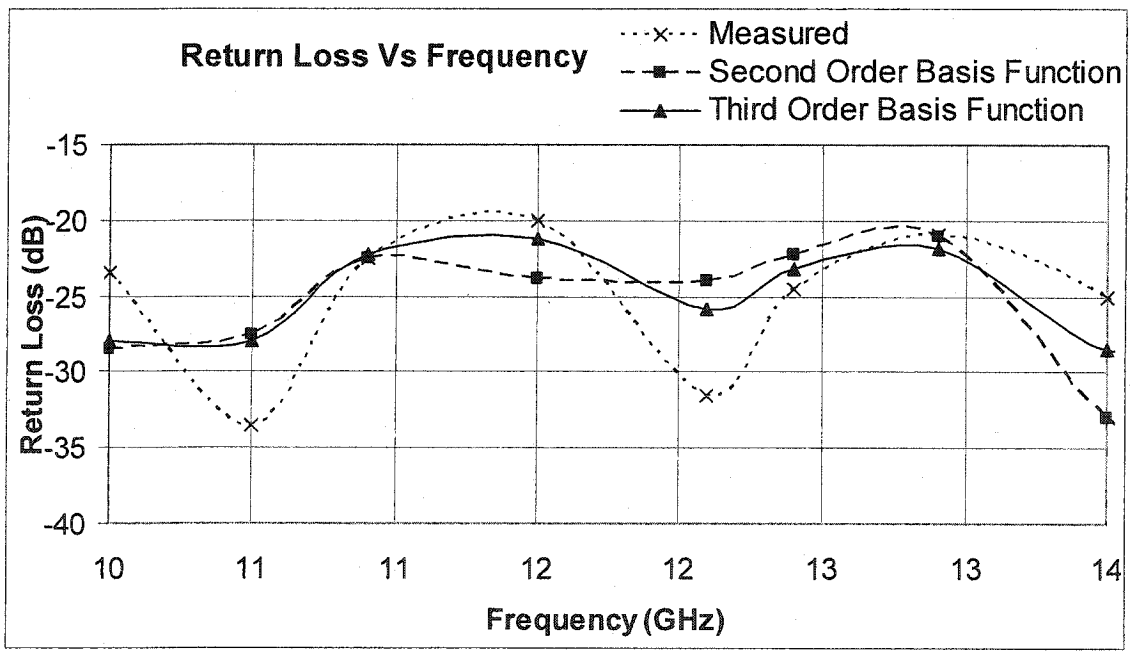

Figure 5-19: Return Loss Vs Frequency.

Figure 5-19 shows the comparison between computed (PML thickness $d_2 = 0.762\,\text{cm}$) and measured Return Loss of the TE_{10} incident mode. From the figure, it is clear that as the order of the basis function increases, computed results become closer to the measured results.

5.5.2 Far Field Radiation Pattern

Finally, the far-field radiation pattern of the PML surrounded horn of section 5.5.1 has been computed. Using the software written for calculating the far field, the normalized radiation pattern has been obtained and compared with the measured result [4].

To make sure the code for the far field works properly, a rectangular aperture as in Figure 5-20 with uniform illumination has been considered.

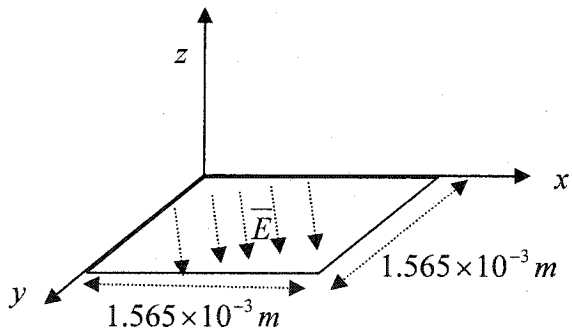

Figure 5-20: Uniformly illuminated aperture

For an aperture field $\overline{E} = 5\hat{a}_x + 10\hat{a}_y\,V/m$, at a distance $r = 100m$ the far-field radiation pattern has been calculated analytically and compared with the computed results. In the far-field, the shape of the field pattern is independent of the distance r as mentioned in section 4.4. In this case, distance $r = 100\,\text{m}$ was just an arbitrary number. Figure 5-21 shows the radiation pattern for the H-plane cut ($\phi = 0$). As each plane has two field components (E_θ and E_ϕ), two separate field patterns are drawn. The computed results for E_θ and E_ϕ as shown in Figure 5-21 (a) and (b) respectively, are almost same as the analytical results. This shows that the code written for far field radiation pattern is working properly.

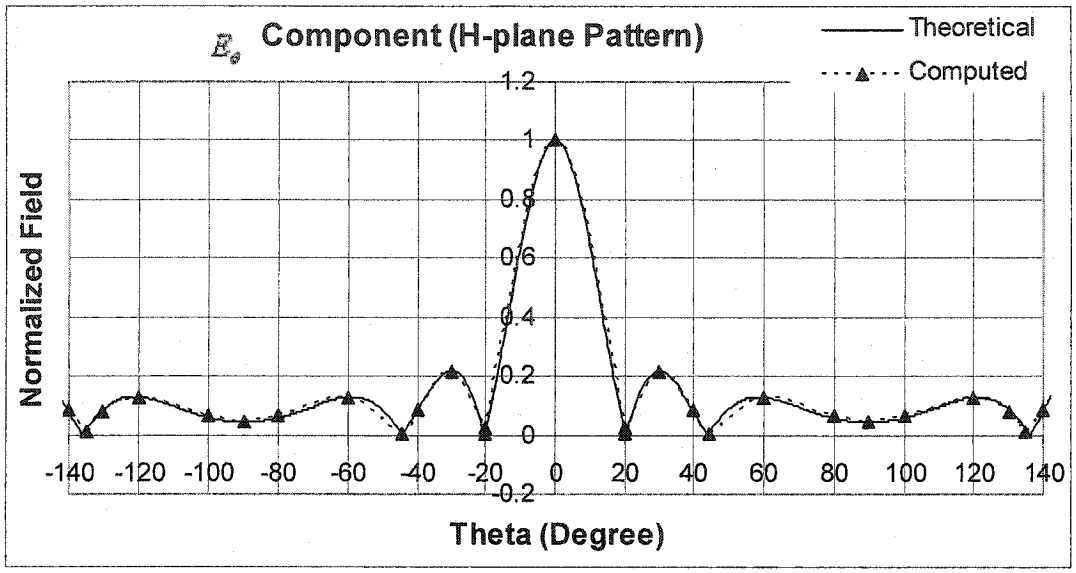

(a)

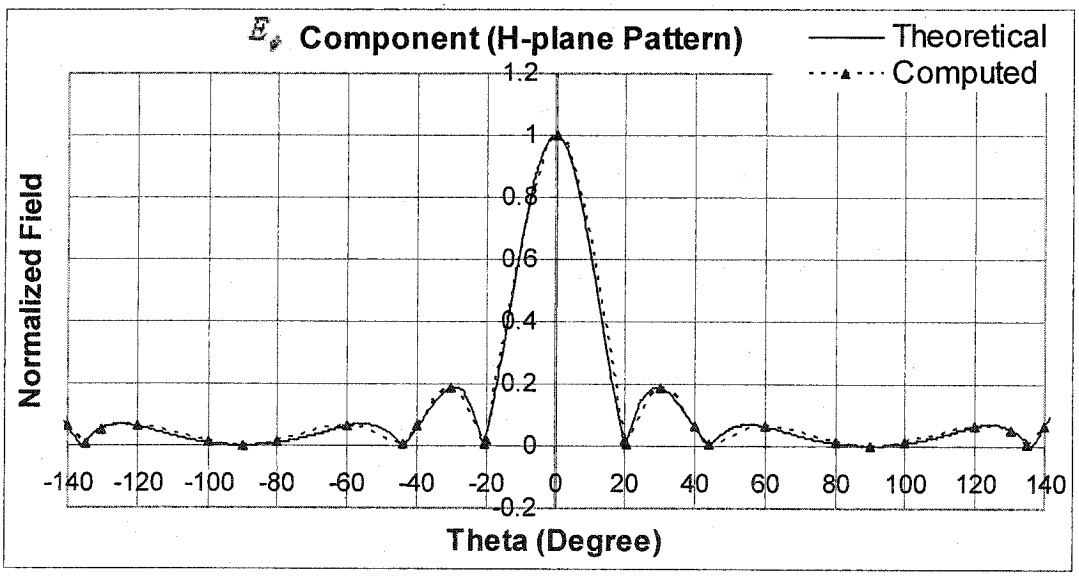

(b)

Figure 5-21: Normalized H-plane Far Field Radiation Pattern.

(a) E_θ component (b) E_ϕ component.

Finally, the far field radiation patterns of the horn has been computed and compared with the measured data. Figure 5-22 shows the radiation pattern for the E-plane cut ($\phi = \frac{\pi}{2}$). As the magnitude of the E_ϕ component of the E-plane is very small (by symmetry it should be zero), only the E_θ component is shown here. There is a discrepancy between the computed and the measured results. As it has already been shown for the uniform

illumination that the program for evaluating far field has been working properly, the error could be due to the field at the horn aperture. Either there is an error in retrieving the correct field from the horn aperture, or/and FE analysis is not computing the correct field at the aperture.

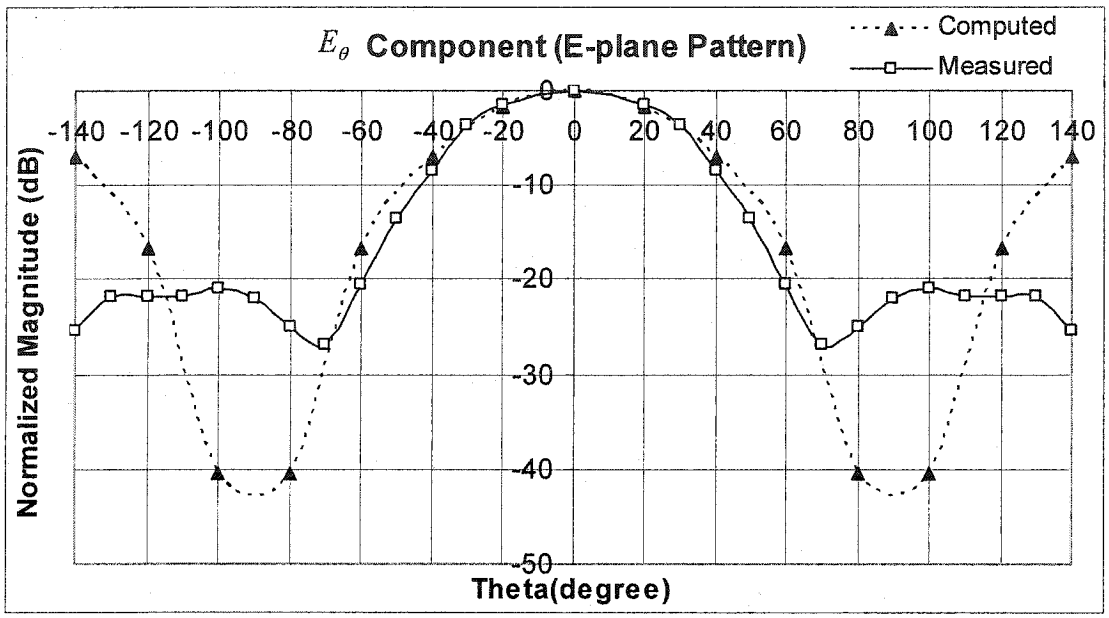

Figure 5-22: Far Field Radiation Pattern for E-Plane cut ($\phi = \frac{\pi}{2}$). E_θ Component.

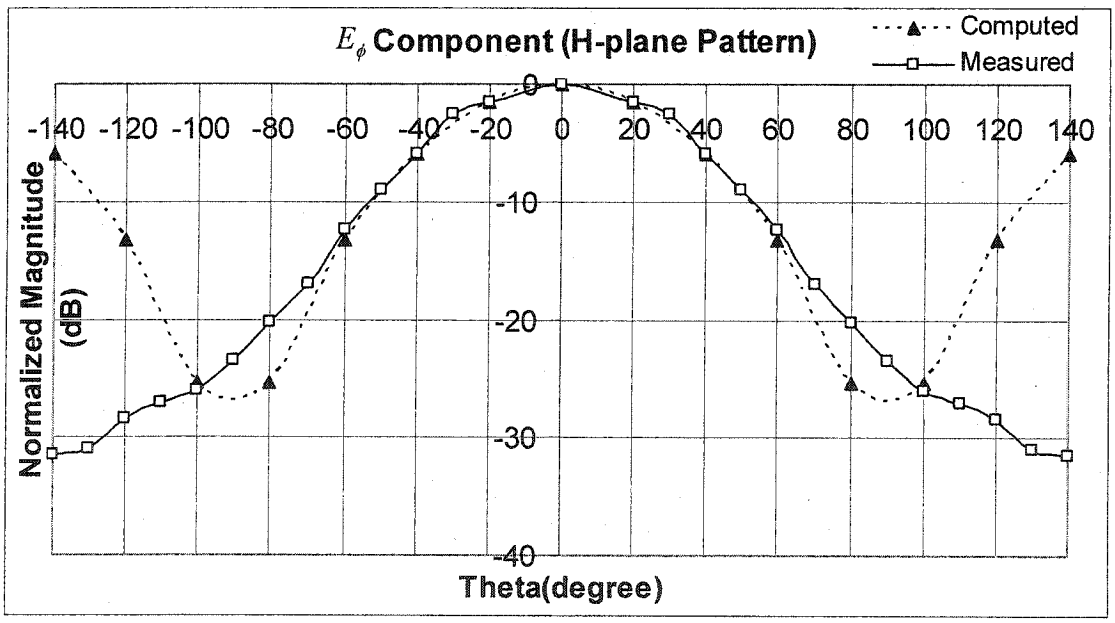

Figure 5-23: Far Field Radiation Pattern for H-Plane cut ($\phi = 0$). E_ϕ Component.

Figure 5-23 shows the radiation pattern for the H-plane cut ($\phi = 0$). As the magnitude of the E_θ component of the H-plane is very small (by symmetry it should be zero), only the E_ϕ component is shown here. The computed pattern does not match with the measured pattern. It could be due to the same reasons as for the E-plane pattern. Due to time constraints this issue could not be solved at this time.

6 Conclusion

The finite element method is one of the most successful frequency domain computational methods for electromagnetic simulations. It combines geometrical adaptability and material generality for modeling arbitrary geometries and materials of any composition. The latter is particularly important in electromagnetics since many applications dealing with antennas, microwave circuits, and scatters, etc. require the simulation of nonmetallic/composite materials. However, open problems, like radiation and scattering, present a unique challenge to finite domain methods. Since the mesh of the computational domain cannot be extended to infinity, boundary conditions must be applied to simulate the effect of infinite domain. The need for efficiently truncating the computational domain for radiation problems is the motivation for the research carried out and described in this thesis. There are several interesting approaches that have been proposed for truncating an infinite computational domain. Among them the PML holds the most promise, as explained in section 1.2.2

In this thesis, an artificial PML with anisotropic material properties was implemented for terminating the FEM mesh for propagation and scattering examples. It was shown that by properly choosing the constitutive parameters, a lossy uniaxial media can be perfectly matched to isotropic space. Unlike Berenger's technique, the PML absorbing media presented here is based on a Maxwellian formulation. It was demonstrated that reasonable performance can be achieved with a relatively thin absorbing layer placed close to the computational domain. From the numerical results, we see that the anisotropic PML can be very effective for scattering problems, provided the appropriate material properties and geometry of the PML are used. It was also shown that the computational efficiency can be improved by carefully considering the relations of the element size and the order of the basis function.

The reflection coefficient of short-circuited rectangular and parallel plate waveguides were computed and compared with the measured results. A good agreement between the results validated the problem set-up and the code used for the FE analysis. Then PML-ended waveguides were studied to investigate the performance of the PML parameters. As the main purpose of this thesis was to analyze open-ended waveguides, a flange terminated rectangular waveguide was studied. The return loss and aperture impedance were computed and compared with the measured results. Finally, a horn terminated rectangular waveguide was studied. The computed return loss agrees well with the measured results. However, there was a discrepancy between the computed and measured far field radiation patterns. The error could have arisen from the aperture field that was used for calculating far field. Due to lack of time this problem could not be solved.

The research was successful for applying the PML and high-order edge elements to horn antennas. But the optimized parameters of the thicknesses of the PML layer, its material properties, and the spacing between the scatter and the PML layer have to be found manually by trial and error. It would be interesting in future to try to come up with some adaptive algorithm so that the program user is not required to have any knowledge of the PML.

7 References

1 Kay, A.F.: 'A wide flare angle horn. A novel feed for low noise broadband and high aperture efficiency antennas'. US Airforce Cambridge Research Laboratories, report 62-757, 1962

2 Oliver, A.D., Clarricoats, P.J.B., Kishk, A.A., and Shafai L: 'Microwave horns and feeds' (IEEE Press, 1994), IEE Electromagnetic Waves series 39

3 Wu, J.-Y., Kingsland, D.M., Lee, R.,Lee, J.-F.: 'A comparison of anispropic PML to Berenger's PML and its application to the finite-element method for EM Scattering', (IEEE Transactions on antennas and propagation, vol. 45, no. 1, January 1997)

4 Battacharyya, A.K.: 'Accurate radiation and impedance characteristics of horn antennas – a moment-method model', (IEEE Transactions on antennas and propagation, vol. 44, no. 4, April 1996)

5 Collin, R.E.: 'Field Theory of guided waves' (McGraw-Hill, New York, 1960, 2nd ed IEEE Press 1991

6 Love, A.W.: 'Electromagnetic horn antennas', (IEEE Press, 1976)

7 Harrington, R.F.: 'Field computation by Moment Method', (New York, Macmillan, 1968)

8 Jin, J.: 'The finite element method in electromagnetics', (New York, Wiley, 1993)

9 Lee, Jin-Fa: 'Advances in finite element methods for microwave engineering'. Proceedings of APMC2001, Taipei, Taiwan, R.O.C.

10 Alfonzetti, S., Borzi, G., and Salerno, N.: 'Iteratively-Improved Robin Boundary Conditions for the finite element solution of Scattering problems in unbounded domains', Int. J. Number Meth. Engng., vol. 42, pp. 601-629, June 1998

11 Jin, J.M., and Volakis, J.L.: 'A finite element-boundary integral method for scattering and radiation by two and three dimensional structures', IEEE Trans. Antennas Propagat., vol. AP-39, pp. 97-104, Jan. 1991.

12 Berenger, J.P.: 'A perfectly matched layer for the absorption of electromagnetic waves', J. Computational Physics, vol. 114, pp. 185-200, 1994.

13 Sacks, Z.S., Kingsland, D.M., Lee, R., and Lee, J.-F.: 'A perfectly matched anisotropic absorber for use as an absorbing boundary condition', ,IEEE Trans. Antennas Propagat., vol. AP-43, pp. 1460-1463, Dec. 1995.

14 Bardi, I., and Cendes: 'New directions in HFSS for designing microwave devices', Microwave Journal, August 1998.

15 Volakis, J.L., Chatterjee, A., and Kempel, L.C.: 'Finite element method for electromagnetics', (IEEE press, New York, 1998).

16 Zienkiewich, O.C., Taylor, R.L.: 'The finite element method' (McGraw-Hill Book Company, 1989)

17 Webb, J.P.: 'Edge elements and what they can do for you', (IEEE Transactions on magnetics, vol. 29, no. 2, March 1993)

18 Webb, J.P., Forghani, B.: 'Hierarchal scalar and vector tetrahedra', (IEEE Transactions on magnetics, vol. 29, no. 2, March 1993)

19 Webb, J.P.: 'Hierarchal vector basis functions of arbitrary order for triangular and tetrahedral finite elements', (IEEE Transactions on antenna and propagation, vol. 47, no. 8, August 1999)

20 Johnk, Carl T.A.: 'Engineering electromagnetic fields and waves (John Willey & Sons, INC., 1988)

21 Gavrilovic, Minya M.: 'Accuracy control optimization of microwave devices by finite element method', (2000)

22 Gavrilovic, Minya M., Webb, J.P.: 'A port element for p-adapitve $S-$parameter

calculation', (IEEE Transactions on magnetics, vol. 35, no. 3, March 1999)
23 Y., Sadd, "Iterative methods for sparse linear systems," (PWS Publishing Company, 1996)
24 Cheng, D.K., "Fields and waves electromagnetics," (Addison-Wesley publishing Company, November, 1992)
25 Infolytica Corp., www.infolytica.ca, Montreal, QC.
26 Microsoft Corp., www.microsoft.com
27 Webb, J.P.: "User Manual for P3Dr", Version 1.3.
28 Kraus, J.D., Marhefka, R.J.: "Antennas for all applications", (Mc Graw Hill, 3rd Edition, 2002)
29 Faires, J.D., Burden, R.: "Numerical method", (PWS-KENT publishing company, Boston, 1993)